Electrical Transport from 5K - 300K in Fe_2O_3@CNT Hybrids

A Thesis

submitted to

Indian Institute of Science Education and Research, Pune

in partial fulfillment of the requirements for the

Master of Science in Quantum Technology

by

Pallavi Pradeep

Indian Institute of Science Education and Research Pune

April, 2026

Supervisor: Dr. Ashna Bajpai

Certificate

This is to certify that this dissertation entitled "Electrical Transport from 5 K - 300 K in Fe_2O_3@CNT Hybrids" submitted towards the partial fulfilment of the Master of Science in Quantum Technology represents work carried out by Pallavi Pradeep from Indian Institute of Science Education and Research Pune under the supervision of Dr. Ashna Bajpai during the academic year 2025–2026.

Signature of Supervisor (Dr. Ashna Bajpai)

Signature of Advisory Member (Dr. Sreejith G.J)

Declaration

I hereby declare that the matter embodied in the report entitled "Electrical Transport from 5 K - 300 K in Fe_2O_3@CNT Hybrids" are the results of the work carried out by me at the Indian Institute of Science Education and Research under the supervision of Dr. Ashna Bajpai and the same has not been submitted elsewhere for any other degree.

Signature of the Author (Pallavi Pradeep)

21/4/26

Date - - - - - -

Acknowledgements

I extend my highest appreciation to Dr. Ashna Bajpai for her constant guidance, encouragement, and support throughout my research work. Her subject matter expertise and her passionate approach to teaching have both helped me develop this research study.

I would like to thank the Department of Physics at Indian Institute of Science Education and Research Pune for providing the necessary facilities, resources, and support that enabled me to conduct my research work.

I sincerely acknowledge Dr. Aparna C and D. Hima Bindu for synthesizing and providing the Fe_2O_3@CNT samples used in this study.

I am also grateful to my peers and lab members for helpful discussions and support during the course of this work.

My heart goes out to my parents and my sister for their resolute encouragement and consistent backing since the very beginning of my kindling academic pursuits. They were there to understand me and support me every time.

I owe heartfelt gratitude to everyone involved in this journey.

Abstract

The material α-Fe_2O_3 (hematite) exists as a stable transition metal oxide which occurs naturally in the environment and displays potential for use in photocatalysis and energy storage. It is also an antiferromagnetic isulator with $T_N \approx 950\,\mathrm{K}$. The α-Fe_2O_3 composite harnesses the synergistic characteristics of CNTs and hematite to achieve better functionality. CNTs function as electrical pathways in Fe_2O_3@CNT composites, while Fe_2O_3 provides active functionality, which results in improved overall system performance.

This thesis examines the structural and electronic transport characteristics of iron oxide–encapsulated carbon nanotube (Fe_2O_3@CNT) composites. It aims to explain how the magnetic properties of hematite (α-Fe_2O_3) core material affect the electrical conduction through carbon nanotube (CNT) networks. Hematite is known to exhibit a spin reorientation transition from pure antiferromagnet to a weak ferromagnetic state. This transition in bulk hematite is known to occur at 260 K. The use of X-ray diffraction (XRD), Raman spectroscopy, and Field Emission Scanning Electron Microscopy (FE-SEM) for structural and morphological analysis indicates that α-Fe_2O_3 exists inside the core cavity of the multiwall CNTs, formed in the aligned forest geometry. This analysis allows one to determine the phase composition, crystallinity, and microstructural characteristics of the composite material. Such CNT network are pressed in the form of a pellet for electrical transport measurements.

The temperature-dependent transport measurements, which was conducted between 5 K and 300 K at different bias currents showed semiconducting behavior. The system exhibited an anomalous behavior, which was identified within the temperature range of 150–300 K. This period matched the Morin transition of the hematite core material in the form of nanoparticles within the core cavity of the CNT.

The Conductivity vs Temperature data is fitted to both the Arrhenius and the Variable Range Hopping model. However, both these models do not seem to adequately explain the transport mechanism in the range of 5K-300K. These data show that the overall features are semiconductor-like with a negative temperature coefficient. More importantly, the Morin transition associated with insulating encapsulate seems to play a role in conduction.

The work shows that electronic transport in Fe_2O_3@CNT composites occurs through multiple mechanisms, which include magnetic transitions, structural heterogeneity, and restricted conduction paths.

Contents

List of Figures

List of Tables

Chapter 1

Introduction

1.1 Carbon nanotubes (CNTs)

Carbon nanotubes (CNTs) have emerged as one of the most promising nanomaterials because they demonstrate exceptional electrical, mechanical, and thermal performance. Since their discovery, CNTs have attracted significant interest in applications that include nanoelectronics, sensors, energy devices, and high-strength materials. Their unique properties develop from their one-dimensional structure and the special bonding patterns that carbon atoms form [1, 2].

Carbon nanotubes (CNTs), as one-dimensional (1D) carbon allotropes, exhibit special physical and electronic characteristics peculiar to low-dimensional materials. Carbon exists in several allotropes with different dimensional structures, including 0D fullerenes, 2D graphene, while bulk crystalline forms, which include graphite and diamond, are 3-dimensional carbon allotropes [3]. Structurally, carbon nanotubes can be visualized as graphene sheets rolled into cylindrical tubes. The structural quality of these materials depends on their synthesis methods, which use Arc discharge, Laser ablation, and Chemical Vapor Deposition (CVD), because higher temperature techniques produce defect-free tubes that sustain their electrical and thermal conductivity [4, 5].

Based on their structure, CNTs can be classified into two main categories which include Single-Walled Carbon Nanotubes (SWCNTs) and Multi-Walled Carbon Nanotubes (MWCNTs).

1.1.1 Single-Walled Carbon Nanotubes (SWCNTs)

SWCNT consists of a single graphene sheet seamlessly wrapped into a cylindrical form. SWCNTs have a typical diameter range that starts from 0.4 nm and extends to approximately 2 nm, while their wall thickness consists of one atomic layer. The 1D tubule structure produces distinct electronic characteristics in the nanotube material which can be both metallic or semiconducting .

The electronic band structure of a SWCNT originated from its hexagonal carbon atom lattice, which connects each carbon atom through sp^2 bonds to three neighboring atoms. The fourth valence electron occupies a p_z orbital which hybridizes with adjacent p_z orbitals to create a delocalized π-band. The tube's conducting properties depend on its translational vector, which is defined as $c_h = n_1 a_1 + n_2 a_2$ [7]. When the index difference

$n_1 - n_2$ shows multiple of three, the nanotube demonstrates metallic properties. The tube exhibits semiconducting behavior through all other situations and maintains a specific band gap value, which exists as E_g [8, 9]. The process leads to a statistical distribution pattern where around 1/3 of fabricated tubes show metallic properties while 2/3 display semiconducting behavior. "Armchair" nanotubes (where $n_1 = n_2$) exist as the only nanotube type which always maintains its metallic properties. "Zigzag" nanotubes show two possible electrical states, which depend on their index values because they can become either metallic or semiconducting [1, 6]. The Luttinger liquid theory replaces traditional Fermi liquid theory in 1D systems because it better describes electron behavior in SWCNTs which experience strong electron-electron interactions and can explain phenomena such as spin-charge separation, the power-law dependencies in electrical conduction, and the reduction of electron tunneling density of states [10, 17].

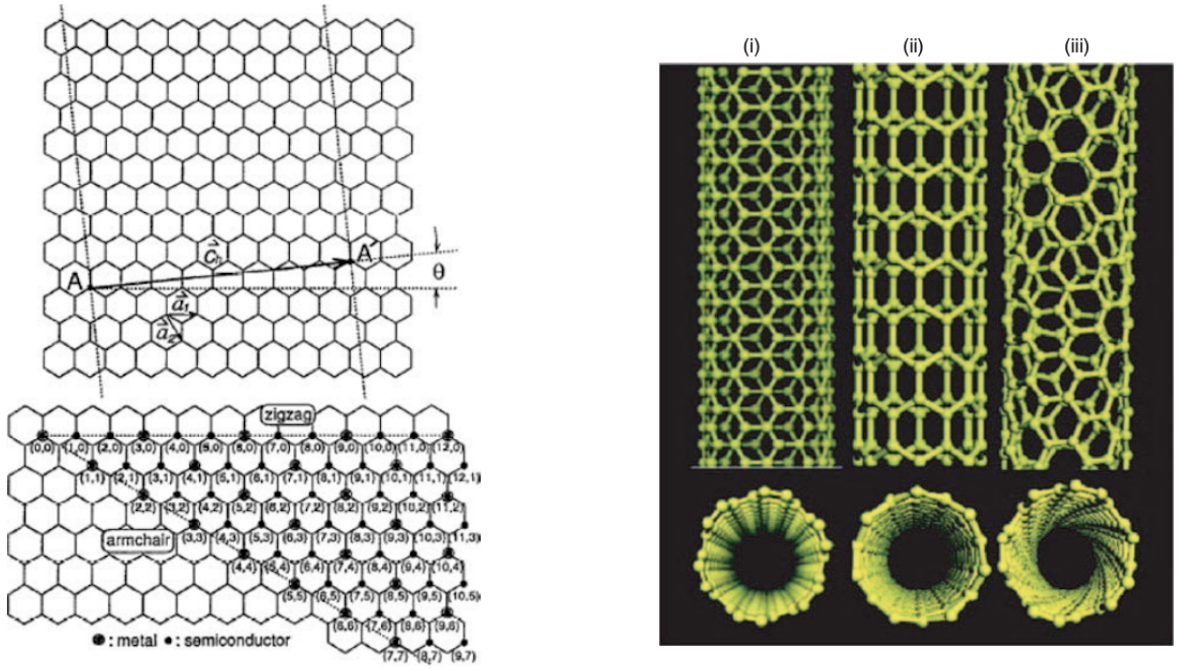

Figure 1.1: (a) The chiral vector representation $\vec{c}_h$ creates the graphene lattice structure which determines whether the resulting SWNT exhibits metallic or semiconducting properties [6] and (b) Visual comparison of (i) Armchair, (ii) Zig-zag, and (iii) Chiral morphologies [1].

The theoretical minimum resistance for a single conduction channel in a SWCNT exists at approximately 6.5 kΩ which matches the quantum conductance limit [11]. Electrons in short nanotubes with mean free paths that exceed nanotube length can move without any scattering which creates ballistic transport. Additionally, SWNTs are highly sensitive to their environment; exposure to ambient oxygen often induces p-type (hole-conducting) behavior, though they can be converted to n-type through vacuum annealing or doping with alkali metals and amine-rich polymers like Polyethyleneimine (PEI) [11, 17].

1.1.2 Multi-Walled Carbon Nanotubes (MWCNTs)

MWCNTs show greater material complexity because their structure consists of multiple graphene tubes that wrap around each other in co-axial configuration. The typical inter-layer spacing between these nested cylinders is approximately 0.34 nm, which closely matches the 0.335 nm inter-planar distance found in bulk graphite [12]. The adjacent layers show different chiralities, which create non-commensurate structures that result in minimal inter-layer electronic coupling, so a single MWCNT can show both metallic and semiconducting shell patterns.

The electronic structure of MWCNTs demonstrates that electrical current flows through the outer nanotube cylinder despite the existence of multiple layers [13]. Experimental evidence from Aharonov-Bohm effect measurements shows that external metal contact geometry contributes to this effect. The mutual interaction between shells must be regarded as a significant factor because armchair-configured MWCNTs show that band crossings create pseudo-gaps in their density of states. The Fermi level in these structures displays strong coupling between electronic states and phonon modes, leading to predictions of superconductivity for these materials [13].

The electrical conductivity of MWCNTs changes according to how the tube diameter (d_t) relates to the elastic mean free path (l_e). The nanotube shows 1D ballistic transport when its diameter remains below the mean free path. Larger diameter tubes typically demonstrate diffusive or two-dimensional transport while smaller diameter tubes show different behavior. The phase coherence length (l_ϕ) serves as a defining characteristic of MWCNT transport, which researchers have measured up to 250 nm, exceeding the tube's actual diameter [11].

The resistance of MWCNT materials shows strong temperature dependence, which results from different methods used to synthesize the materials. The arc-discharge method of high-temperature growth produces cleaner nanotubes, which display metallic properties because their resistance drops in a linear pattern as temperature increases. The CVD-grown tubes show disordered behavior, which leads to weak localization at low temperatures (below 60 K), where their conductance starts decreasing at a logarithmic rate until it reaches a steady state.

MWCNTs demonstrate several advanced quantum interference effects when subjected to magnetic fields. Ballistic transport with quantized conductance (multiples of $G_0 = 2e^2/h$) has been observed at room temperature, particularly when using quasi-liquid contacts like mercury to ensure perfect transmission [14]. The accurate measurement of intrinsic conductivity faces challenges because contact resistance at the metal-nanotube interface restricts measurements while poor Ohmic contacts create severe problems that impact the transport behavior assessment [14, 17].

Magnetoresistance measurements provide important information about electron trans-

port in MWCNTs. In the presence of a magnetic field, quantum interference effects can modify the conductance. In disordered nanotubes, weak localization occurs, leading to a decrease in conductance at low temperatures. This is often accompanied by negative magnetoresistance, where the magnetic field suppresses interference and increases conductance.

Magnetotransport experiments also reveal universal conductance fluctuations with a characteristic magnitude of e^2/h [16]. Another key phenomenon is the Aharonov-Bohm effect, where magnetic flux through the nanotube changes the electron phase, producing periodic conductance oscillations and indicating that current mainly flows through the outermost shell of the MWCNT [15, 17].

1.2 Magnetism in Materials

Magnetism exists as a collective phenomenon because all electrons possess a magnetic moment. The atom is the fundamental component of all matter, containing electrons that generate magnetic attributes in the substance. The electron magnetic moment results from two types of motion: spin motion and orbital motion around the nucleus. The Faraday law of magnetic induction states that when a material enters a magnetic field, its embedded electrons experience magnetic forces [18]. The atomic and molecular structure of materials determines how they respond to external magnetic fields, while their total magnetic moment governs this process. An atomic system shows its total magnetic moment through its electron arrangement because paired electrons produce opposing spins, which eliminate their magnetic fields, whereas unpaired electrons create a total magnetic moment that strongly responds to external magnetic fields [19].

Materials magnetic behavior is characterized through the relationship between magnetic induction (B) and applied magnetic field (H), and shows linear dependence as $B = \mu H$, with magnetic permeability μ as the defining element. The magnetic susceptibility describes the magnetic field response of a material, given by $\chi = \mu - 1$ [18, 19].

1.2.1 Diamagnetism

Diamagnetism occurs in materials that do not have unpaired electrons or have their orbitals filled, resulting in a zero magnetic moment in the absence of an external field. Michael Faraday discovered this property of diamagnetic materials in the year 1845. The materials show only a minor magnetic field response. The orbital angular momentum of electrons produced by the field moves in the opposite direction, a phenomenon consistent with Lenz's Law. Hence, the diamagnetic materials show a negative magnetic moment. Water, acetone, copper, and carbon dioxide serve as examples of diamagnetic materials. The material has a negative magnetic susceptibility of the order 10^{-5} and permeability

(μ) of less than unity [7, 21].

1.2.2 Paramagnetism

The magnetic behavior of paramagnetic materials occurs due to their unpaired electrons, which impart a magnetic moment to each atom. The atomic moments are randomly oriented in the absence of an external magnetic field due to thermal energy agitation, which leads to zero net magnetization. However, upon applying a magnetic field, dipoles create a small positive magnetization because they align with the magnetic field direction. The magnetic susceptibility (χ) of paramagnetic materials like aluminum, calcium, and oxygen falls within the range of 10^{-5} to 10^{-3}. The susceptibility of this material exhibits temperature dependence because it follows Curie's Law, which states that magnetization decreases when absolute temperature increases according to the equation $\chi = C/T$ [20, 21].

1.2.3 Ferromagnetism

Ferromagnetic materials, which include iron, cobalt, and nickel, create a unique magnetic material category because these materials display high magnetic field response and maintain their magnetic properties. The phenomenon occurs because exchange interaction, a quantum mechanical effect, causes adjacent atomic magnetic dipoles to couple and align parallel to one another [20]. The Hamiltonian for exchange interaction for ferromagnets can be described as:

$$H = \sum_{i,j} J_{ij} \mathbf{S}_i \cdot \mathbf{S}_j \tag{1.1}$$

where J_{ij} is the exchange integral which defines the strength of coupling between moments at two moments i and j. The exchange integral for ferromagnetic materials maintains positive values at all times [22, 23].

The main characteristic of ferromagnetism includes magnetic domains, which exist as tiny regions that contain atomic dipoles pointing in a single direction. The magnetic moments of these different domains point in random directions when the system remains unmagnetized, resulting in the total magnetization that equals zero. The application of an external field causes the domains to rotate and align together, leading to high saturation magnetization. The alignment stability of this system depends on temperature variations. The Curie temperature of each ferromagnetic material defines its specific threshold point at which thermal energy will disrupt exchange interaction, which leads to the material's conversion into a paramagnetic state. The material exhibits hysteresis below the Curie temperature because its magnetization lags behind magnetic field variations, which enables it to function as a permanent magnet. Ferromagnetic materials demonstrate exceptional magnetic susceptibility values that range from 10^3 to 10^5

because of their strong internal couplings [20].

1.2.4 Anti-ferromagnetism

Antiferromagnetism occurs when the magnetic moments of atoms or ions align in a regular pattern with neighboring spins pointing in opposite directions resulting in one sub-lattice with up spins and another sub-lattice with down spins. The exchange integrals show positive values within one sublattice but show negative values for coupling with respect to other sublattices. The presence of oxygen in many oxides creates isolated magnetic ions, which result in antiferromagnetic ordering through the indirect exchange mechanism known as Superexchange [23].

The magnetic moments from both sub-lattices in a perfectly antiferromagnetic material reach equal magnitude but display opposing magnetic directions; the two components completely nullify each other, which results in no magnetic moment present when there is no external magnetic field. The state remains intact until the temperature reaches the critical point known as the Néel temperature (T_N). The material transforms into a paramagnetic state when the temperature crosses T_N because thermal energy breaks the antiparallel magnetic order. Antiferromagnetic materials show a small positive magnetic susceptibility value and a magnetic permeability value. Common examples of materials exhibiting this behavior NiO and α-Fe_2O_3 [20].

1.2.5 Ferrimagnetism

Ferrimagnetism occurs mainly in complex magnetic oxide materials, which include ferrites and magnetite. The spin structure of this material also consists of sub-lattices which exhibit antiparallel magnetic moments, just like antiferromagnetism does. The essential difference between the two exists because ferrimagnetic materials possess two opposing magnetic moments, which differ in magnitude. The material demonstrates spontaneous magnetic behavior because its up and down spins fail to achieve complete cancellation. This ordering persists until the material reaches the critical point known as the Néel temperature (T_N). The material transforms into a paramagnetic state because thermal energy above this temperature causes destruction of its alignment. Ferrimagnetic materials display a strong positive magnetic susceptibility, which enables them to respond effectively to external magnetic fields. This property makes them vital components in high-frequency electronic devices and permanent magnets [20, 24].

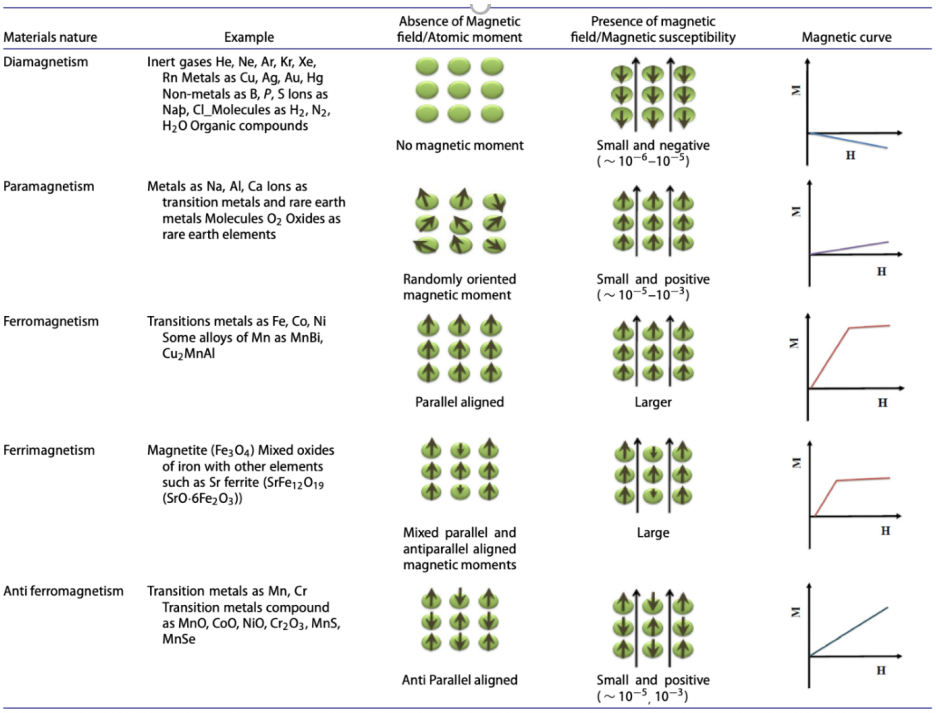

Figure 1.2: Fundamental types of magnetism, taken from [20].

1.2.6 Weak Ferromagnetism

Weak ferromagnetism exists as a distinct phenomenon that occurs in particular antiferromagnetic (AFM) crystals that include α-Fe_2O_3 and $MnCO_3$ because these crystals maintain a slight spontaneous magnetization [25]. The early theories, which explained this phenomenon as a result of defects or impurities, until Dzyaloshinskii and Moriya demonstrated through theoretical research that the phenomenon exists as an inherent characteristic governed by crystal symmetry and quantum mechanical interactions [25].

The standard collinear antiferromagnet has its sub-lattice spins aligned antiparallel, which produces a total magnetic moment of zero. Uniaxial crystals exhibit a special behavior where their sub-lattice magnetization remains perpendicular to the main symmetry axis through which their spins achieve a slight canting effect. The departure from complete antiparallelism results in partial magnetic cancellation, which produces a small but measurable ferromagnetic moment [25, 26].

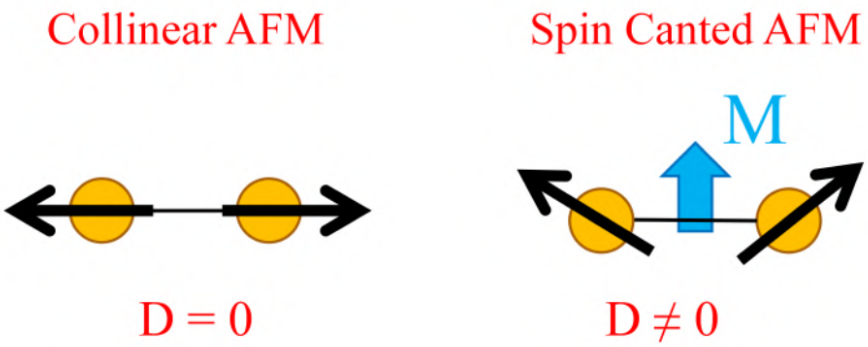

Figure 1.3: Collinear and Canted Antiferromagnet

Dzyaloshinskii demonstrated that in uniaxial crystals, this canting is allowed by symmetry when the sub-lattice magnetization is perpendicular to the principal symmetry axis (e.g., the [111] axis in hematite). The material reaches its pure antiferromagnetic state when the spins align parallel to this axis, as they do in α-Fe_2O_3, where canting vanishes at temperatures below the Morin transition, which occurs at 260 K [25].

Moriya combined the Heisenberg superexchange model, which describes hopping of electron to different sites with spin-orbit coupling (SOC) to give a microscopic explanation [26]. The Dzyaloshinskii-Moriya Interaction (DMI) emerges as an antisymmetric exchange interaction which is expressed through the Hamiltonian:

$$H = -J_{ij}\mathbf{S}_i \cdot \mathbf{S}_j + \mathbf{D}_{ij} \cdot (\mathbf{S}_i \times \mathbf{S}_j), \tag{1.2}$$

where $\mathbf{D}$ represents the Dzyaloshinskii-Moriya vector.

The phenomenon of weak ferromagnetism (WFM) does not exist as a universal property that all antiferromagnetic materials share despite their identical crystal structures. The comparison between hematite α-Fe_2O_3 and chromium oxide Cr_2O_3 serves as an excellent example. The two substances share a rhombohedral unit cell, which contains four magnetic ions that extend along the [111] body diagonal. The material α-Fe_2O_3 shows a spontaneous WFM moment which exists between its Néel temperature ($T_N = 950$ K) and its Morin transition ($T_M = 260$ K), while Cr_2O_3 stays as a complete antiferromagnet (AFM) throughout its full ordered state [25–27].

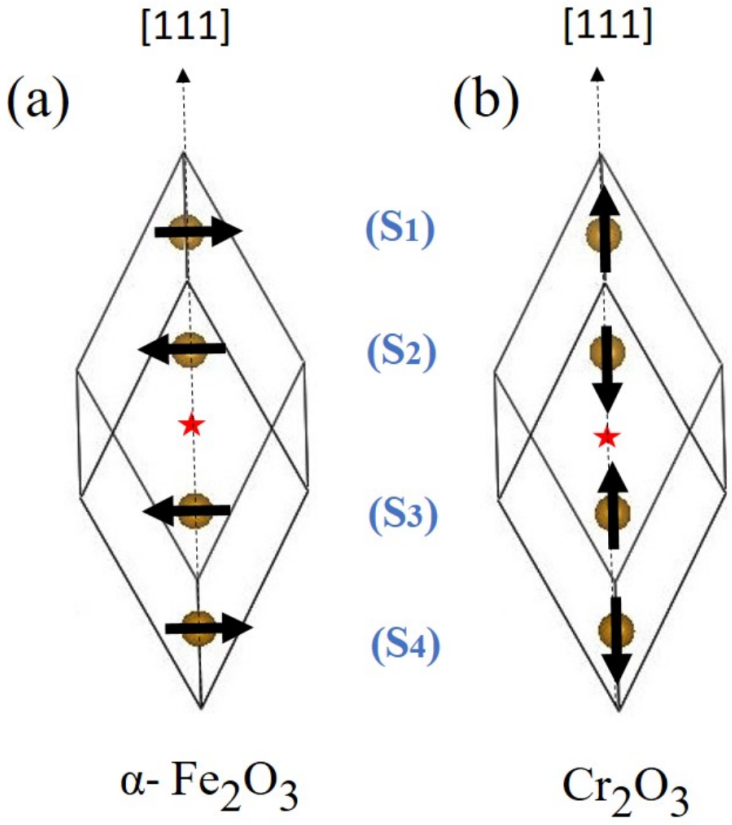

Figure 1.4: The antiferromagnetic spin arrangement of α-Fe_2O_3 and Cr_2O_3 exists below their T_N temperature. The inversion centers of the unit cell are indicated by star marks which appear as ($\star$).

The fundamental difference lies in the spin configurations:

In Cr_2O_3, the spins establish two separate spin groups which develop their directional relationship through the equation $\mathbf{S}_1 \parallel \mathbf{S}_3$ and $\mathbf{S}_2 \parallel \mathbf{S}_4$. The specific spin arrangement leads to total DMI Hamiltonian cancellation which results in $H_{\mathrm{DM}}(Cr_2O_3) \equiv 0$.

In α-Fe_2O_3, the spins align as $\mathbf{S}_1 \parallel \mathbf{S}_4$ and $\mathbf{S}_2 \parallel \mathbf{S}_3$. The DMI term exists in this configuration as $H_{\mathrm{DM}}(\alpha\text{-}Fe_2O_3) = 4\mathbf{D} \cdot (\mathbf{S}_1 \times \mathbf{S}_2)$. The presence of DMI remains active, which causes the WFM phase to exhibit its typical spin canting behavior as long as the two vectors $\mathbf{S}_1$ and $\mathbf{S}_2$ maintain their non-perfect (anti)parallel relationship.

The temperature drop at T_M in α-Fe_2O_3 initiates a spin reorientation transition process. In this pure AFM phase, the spins, while still coupled in the $\mathbf{S}_1 \parallel \mathbf{S}_4$ fashion, realign to point strictly along the [111] rhombohedral axis. The spins have reached a state where their direction matches the $\mathbf{D}$ vector, which results in $(\mathbf{S}_1 \times \mathbf{S}_2)$ becoming zero. The DMI vanishes because the geometric alignment leads to the complete elimination of the weak ferromagnetic moment [25, 26, 28].

The relationship between the antiferromagnetic vector ($\mathbf{l} = \mathbf{S}_1 - \mathbf{S}_2$) and the magnetization vector ($\mathbf{m} = \mathbf{S}_1 + \mathbf{S}_2$) further clarifies the characteristics of this magnetic behavior.

The DMI can be rewritten as [29]:

$$\mathbf{D} \cdot (\mathbf{S}_1 \times \mathbf{S}_2) = \frac{1}{2}\mathbf{D} \cdot (\mathbf{l} \times \mathbf{m}) \tag{1.3}$$

The mathematical relationship demonstrates that the WFM vector ($\mathbf{m}$) maintains a right angle to the AFM vector ($\mathbf{l}$), which defines it as *transverse weak ferromagnetism*. In contrast, *longitudinal weak ferromagnetism* occurs when $\mathbf{m}$ is parallel to $\mathbf{l}$. The latter form of the phenomenon results from Single Ion Anisotropy (SIA), which occurs because of crystal field differences and spin-orbit coupling (SOC) at various magnetic locations [26,30]. The DMI leads the magnetic profile because it produces first-order effects through SOC, while SIA functions as a second-order effect [26].

1.3 Hematite (α-Fe_2O_3)

Transition metal oxides are of interest because they exhibit new physical, magnetic, and optical properties that appear when they reach nanoscale dimensions. The properties of this material differ from its bulk properties because it exhibits high surface-to-volume ratios, finite size effect, and quantum confinement effects. The oxide materials include sixteen different iron oxide forms, which exist as the most significant group among the various oxide materials [31,33,34]. Magnetite (Fe_3O_4), hematite (α-Fe_2O_3), and maghemite (γ-Fe_2O_3) represent the most studied materials because they show superior structural and magnetic stability [35]. Hematite stands out as the best choice because it exists in nature as an abundant material that has low toxicity and maintains its chemical composition. The material shows extensive applications because it possesses biocompatibility together with excellent catalytic performance and its ability to react sensitively to external magnetic fields [35].

Hematite exists as the most thermodynamically stable iron oxide mineral, which occurs naturally in the environment. It is an n-type semiconductor at room temperature [20] and is used as a precursor for synthesizing magnetite and maghemite. Structurally, Hematite displays a rhombohedral corundum-type lattice structure, which belongs to the space group $R\bar{3}c$. The system contains Fe(III) ions, which occupy two-thirds of all available octahedral positions throughout the hexagonal close-packed (hcp) oxygen lattice structure. The material exhibits specific atomic arrangements that determine its electronic transport capacity and its magnetic characteristics [36]. Hematite possesses a narrow bandgap of approximately 2.2 eV. The electronic structure of the material consists of a conduction band, which arises from the unoccupied 3d orbitals of Fe(III) ions, whereas the valence band contains occupied 3d crystal field orbitals together with substantial 2p non-bonding orbital elements from oxygen [33].

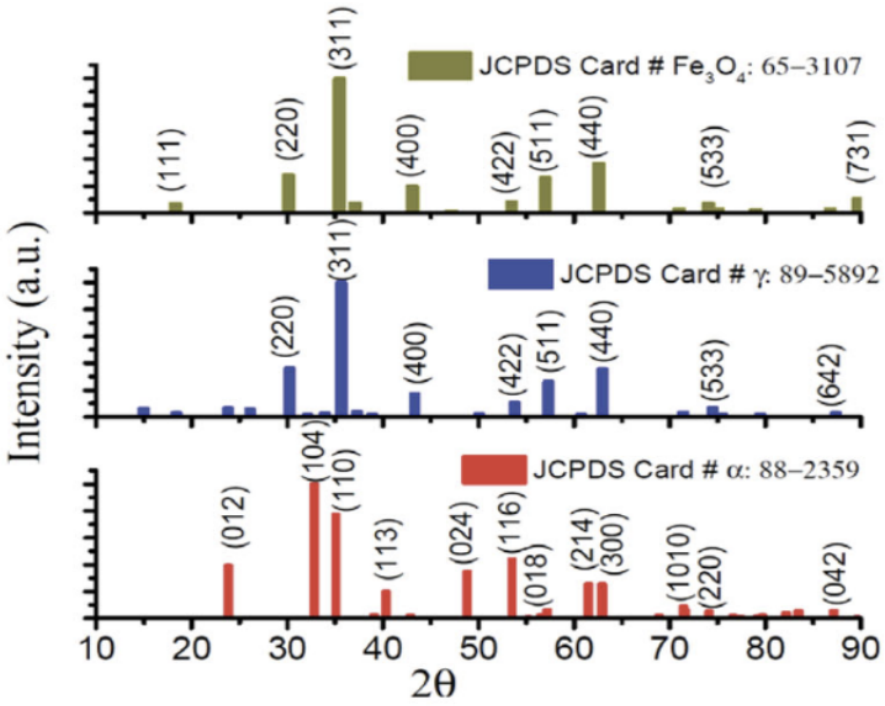

Figure 1.5: The powder diffraction patterns are in accordance with JCPDS data cards for α-Fe_2O_3, γ-Fe_2O_3 and Fe_3O_4 [20].

Hematite undergoes antiferromagnetic ordering at temperatures below its Néel point, which is approximately 960 K. The Morin transition occurs at approximately $T_M = 260\,\mathrm{K}$ which defines the main characteristic of bulk hematite because it causes the material to change its direction of magnetic alignment. The material exists in an antiferromagnetic phase, which exists until T_M because its two antiparallel sublattice spins are aligned strictly along the rhombohedral [111] axis. The material enters a weak ferromagnetic state when temperatures exceed T_M because its spins now move toward the basal (111) plane while undergoing minor canting. The transition between states occurs because the total magnetic anisotropic constant undergoes a total change from positive to negative, which happens when reaching the T_M point.

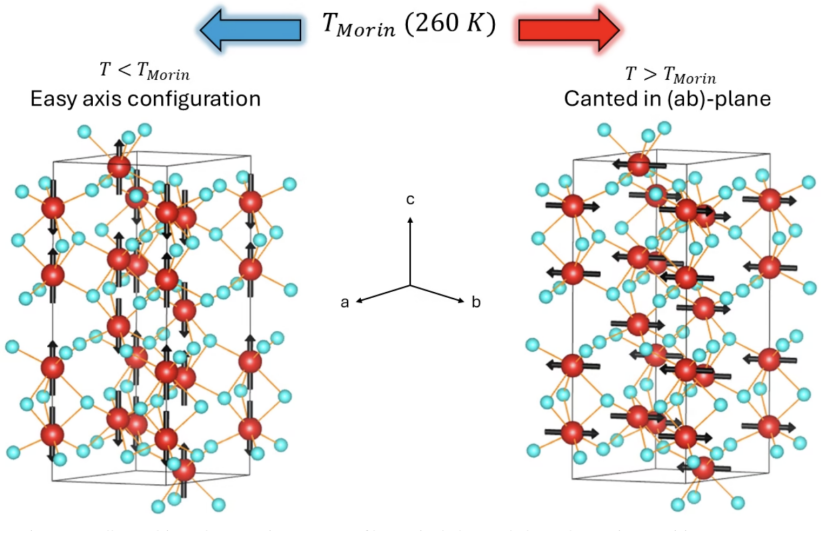

Figure 1.6: Schematic representation of the magnetic spin reorientation in α-Fe_2O_3 at the Morin transition (T_M), illustrating the shift from c-axis alignment ($T < T_M$) to the basal ab-plane ($T > T_M$).From [32]

The magnetic properties of this material depend on the external magnetic field, which creates two distinct effects that include spin-flip transitions and changes in Morin transition temperature when the field aligns with or against the [111] axis. Theoretical models of the field-induced AF-WF transition use Dzyaloshinsky's phenomenological thermodynamical potential because it describes how exchange interactions and anisotropy create their complex phenomena [33].

Chapter 2

Experimental Methods

The synergy between iron oxide nanoparticles and their carbon nanotube framework needs assessment through multi-scale methods. The chapter provides an overview of fundamental principles which serve as the basis for all techniques that are employed in this work. The study investigates three analytical methods, which include X-ray diffraction (XRD) for phase and structural analysis, Raman spectroscopy for vibrational and defect characterization and Scanning Electron Microscopy (SEM) for morphology assessment. The working principle of the Closed Cycle Refrigerator (CCR) used for temperature-dependent transport measurements is also briefly discussed.

2.1 X-Ray Diffraction (XRD)

XRD serves as a fundamental analytical method in materials science because it reveals exceptional details about the crystalline structure of materials through X-ray radiation interacting with their internal atomic arrangement. The technique produces characteristic patterns of intensity versus diffraction angle (2θ) which serve as unique fingerprints for crystalline materials. The patterns develop from constructive X-ray interference, which occurs when X-rays scatter off atoms that exist in a specific periodic pattern, this phenomenon follows Bragg's Law, which states that:

$$2d \sin\theta = n\lambda \tag{2.1}$$

where n represents the order of reflection, λ denotes the X-ray wavelength, d stands for interplanar spacing, and θ indicates the diffraction angle.

Crystalline materials generate sharp peaks because their atomic structure consists of regular repeating 3D patterns, while amorphous materials produce broad diffuse scattering patterns because their atomic structure lacks defined order [37].

The Scherrer equation determines crystallite size through the formula:

$$D = \frac{k\lambda}{\beta \cos\theta} \tag{2.2}$$

where D represents the crystallite size, the Scherrer constant k has a standard value of 0.9, λ denotes the X-ray wavelength, β represents the peak width at half maximum, and θ indicates the Bragg angle [37].

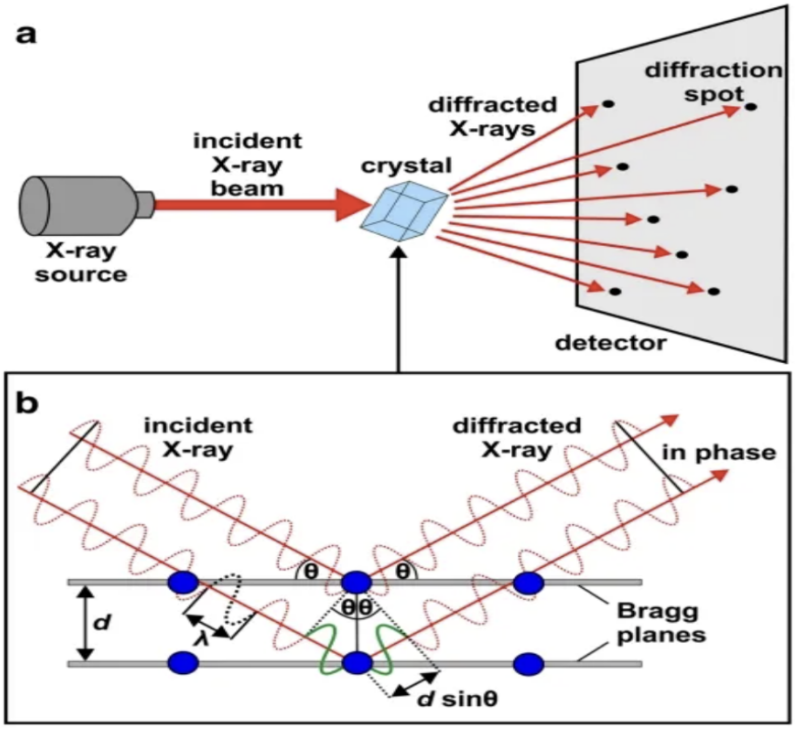

Figure 2.1: X-ray Diffraction Experiment [38].

Peak width reflects crystallinity: perfect single crystals with long-range order yield sharp peaks, whereas poor crystallinity or small crystallite size causes broadening. Three primary factors create this broadening: Scherrer broadening from finite crystallite size and microstructural defects, which include vacancies, dislocations, and stacking faults that disrupt periodicity and microstrain, which creates a range of d-spacings.

The peak position is affected by strain, which helps identify macrostress that extends over large distances and microstress, which changes from one grain to another. The interplanar spacing increases with uniform tensile strain, which causes peak shifts to lower 2θ angles, and the interplanar spacing decreases with uniform compressive strain, which results in peak shifts to higher 2θ angles. The peak broadening occurs when non-uniform strain develops across a grain which results from the sum of the sharp lines [37].

Doping introduces impurities that cause lattice expansion or contraction, which leads to changes in lattice parameters that produce strain, which results in XRD peak shifts. The lattice expands when large foreign atoms are used for substitutional doping, which results in leftward peak shifts, while smaller dopants cause contraction, which results in rightward peak shifts, yet the crystal structure remains constant through changes in lattice parameters. Interstitial doping enters foreign atoms into spaces between host atoms, which creates potential for both lattice parameter and crystal structure changes that produce peak shifts, together with potential structural modifications. Bragg's law indicates that expansion of d value leads to lower diffraction angles, which results in

leftward shifts, while contraction of d value produces higher diffraction angles, which results in rightward shifts. The excessive doping process may result in solubility limits being surpassed, which causes secondary phase creation that includes Al_2O_3 in Al-doped ZnO, which shows up as new peaks within the XRD pattern [37].

2.2 Scanning Electron Microscopy (SEM)

Field-Emission Scanning Electron Microscopy (FESEM) was used to study the surface morphology and structural characteristics of the metal and metal-oxide materials within the carbon nanotubes. The Field Emission Scanning Electron Microscope (FESEM) functions as a powerful instrument that generates high-resolution pictures through its electron imaging mode to observe features that traditional optical and thermionic scanning microscopes cannot detect. The system goes beyond its imaging functions by using characteristic X-rays to analyze elemental composition through Energy Dispersive X-Ray (EDX) analysis. The method produces qualitative and quantitative data about specific areas of the sample surface because different chemical elements emit unique scattered X-ray energy. The study in this thesis used a ZEISS ULTRA plus instrument for its research experiments.

The fundamental principle of electron microscopy involves the interaction of a high-energy electron beam with the atoms of a sample. The incident beam produces multiple signals after it contacts the surface of the sample [40].

- **Secondary Electrons (SE):** These are low-energy electrons that surface atoms release after they undergo inelastic scattering. They are primarily used to map the topography and surface features of the sample.

- **Back-Scattered Electrons (BSE):** These are all electrons which start as incident electrons but bounce back from the atomic electron cloud. The scattering cross-section of BSEs is highly dependent on the atomic density (atomic number, Z) of the material. Higher atomic density areas generate brighter visual output which enables users to achieve high-contrast compositional resolution.

- **Characteristic X-Rays:** When secondary electrons are ejected from the inner shells of an atom, electrons from higher-energy outer shells drop down to fill the vacancies. This transition releases X-ray photons with energy levels corresponding to the difference between the shells. The analysis of these elemental specific wavelengths allows for precise elemental identification.

An electron gun together with scanning coils and electromagnetic lenses forms the basic components of a standard SEM setup. The electron beam moves through deflection

plates and scanning coils before passing through the last lens system, which uses raster scanning to direct the beam onto the sample. The detectors capture the emitted signals, which they amplify to produce an intensity distribution map or image. Scientists use conductive materials for sample preparation because static charge accumulation requires conductive samples, while non-conducting samples need a thin gold or carbon layer that is applied through sputter coating.

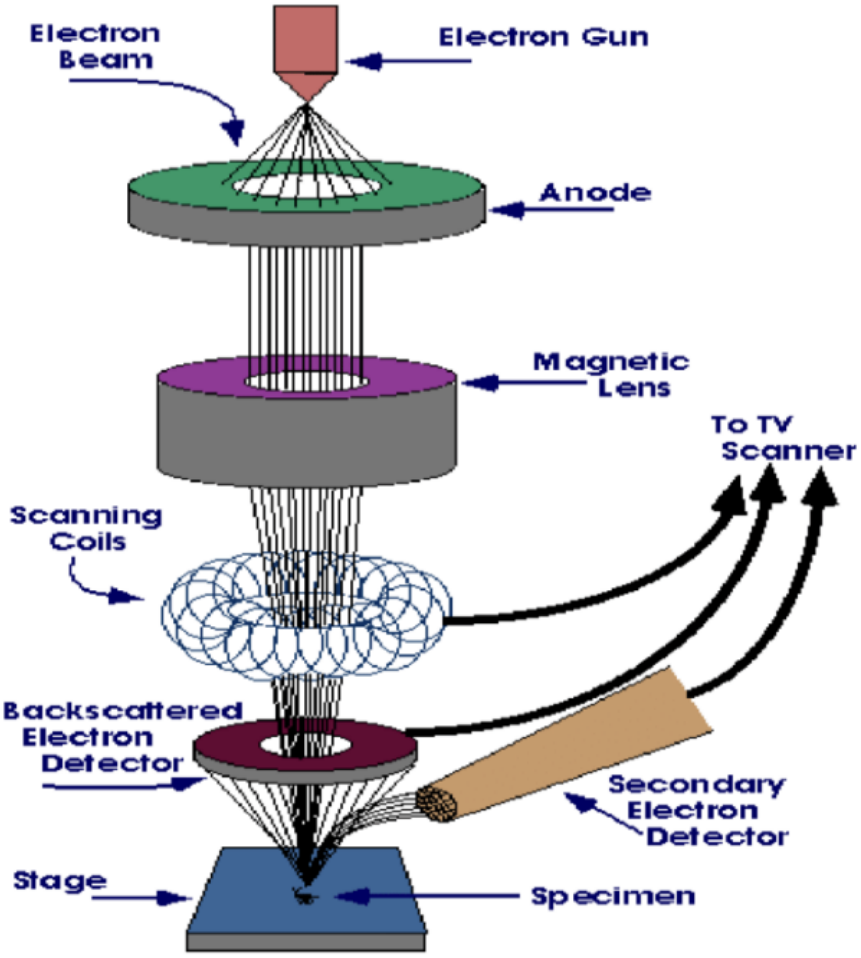

Figure 2.2: Schematic representation of FESEM instrument. From [39].

FESEM distinguishes itself from other systems through its Field Emission Gun (FEG) source, which produces a more concentrated and coherent electron beam than thermionic emitters. The system achieves better spatial resolution, which enables users to create high-quality images through low voltage operation that ranges from 0.02 kV to 5 kV. The system uses low voltages because they diminish charging effects on non-conductive samples, which combined with specialized in-lens detectors, allow researchers to study fragile nanostructures without causing major harm to samples [40].

The analysis requires specific beam energy settings, which use low-energy beams be-

tween 5 keV and 10 keV to produce surface topography results and require Energy Dispersive Spectroscopy (EDS) to use higher energy levels between 15 keV and 20 keV for X-ray activation. At least one excitation energy level must exceed the absorption edge of all elements under investigation. The research team used conductive carbon tape to secure powder specimens onto their mounting platform for stable imaging.

2.3 Raman Spectroscopy

Light interacts with materials through three possible outcomes, which include transmission, reflection, and scattering. Raman spectroscopy serves as a powerful method to probe vibrational modes while obtaining chemical and structural information through the inelastic scattering of monochromatic light [44].

The interaction of a laser beam with a molecule causes its electromagnetic field to oscillate, which induces the electron cloud to become polarized, resulting in the molecule reaching a temporary virtual state. As this state is unstable, the molecule relaxes by emitting a scattered photon. The majority of photons undergo Rayleigh scattering, which results in no energy change during the scattering process. A small fraction of the light undergoes inelastic scattering through the Raman effect, which causes the scattered photons to have different energy levels compared to the incoming photons because they interact with molecular vibrational modes [43, 44].

The process of Stokes scattering occurs when the scattered photon energy remains below the energy of the incident photon because the process transfers energy from the photon to the molecule. Anti-Stokes scattering occurs when the scattered photon energy exceeds the incident photon energy because the molecule transfers energy to the photon. The vibrational state populations determine the relative strengths of these processes which therefore change according to temperature and excitation conditions [44].

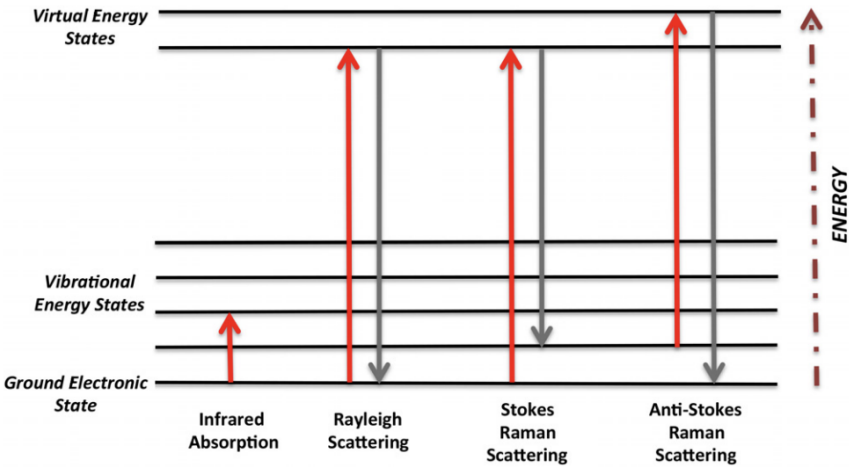

Figure 2.3: Energy level diagrams for Rayleigh & Raman scattering. From [43].

A standard Raman spectrometer includes a laser system that generates excitation light and optical devices that transmit pure monochromatic light and uses a spectrograph system to detect light intensity across different wavelengths and employs a microscope system to direct laser light onto the testing sample. The system operates through computer-based control, which manages both data collection and data evaluation processes [43].

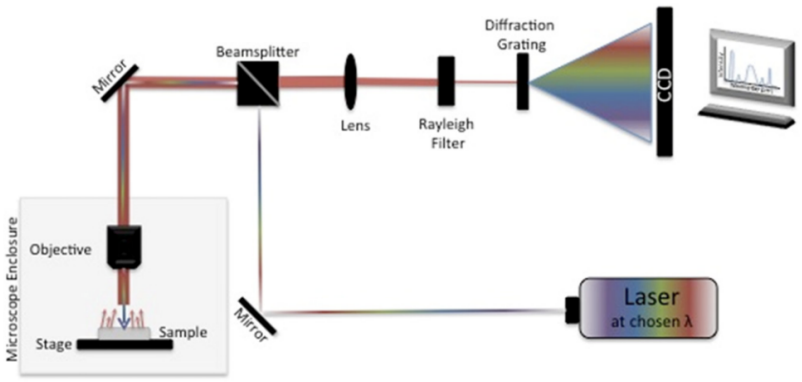

Figure 2.4: Schematic representation of a Raman spectrometer instrument [43].

2.4 Closed-Cycle Refrigerators (CCR)

Closed-cycle refrigerators have emerged as essential systems for cooling devices for characterizing the optical, electrical, and magnetic properties of materials. CCR systems operate with a closed-loop helium gas system instead of using cryogens like open systems do, achieving operational temperatures from 4 K to 300 K in small laboratory settings.

The ARS closed-cycle cryostat functions through a Gifford-McMahon (GM) refrigeration cycle. The cryostat uses internal pressure differentials to drive its displacer system,

which results in lower mechanical vibrations, making it suitable for delicate optical spectroscopy work [41].

A high-performance CCR setup integrates several specialized components to maintain a stable, ultra-low temperature environment. The closed-cycle cryostat system consists of four main parts, which include the expander, compressor, together with the vacuum shroud and radiation shield. The Gifford-McMahon refrigeration cycle takes place in the expander, which is commonly referred to as coldhead or cold finger. The system establishes a connection to a compressor through two gas lines and an electrical power cable. The gas line system consists of two pipes, which first carries high pressure helium gas to the expander and then returns low pressure helium gas from the expander. The compressor delivers helium gas at both high and low pressure to the expander, which uses this gas to produce the required refrigeration output. The vacuum shroud creates a vacuum around the cold end of the expander to prevent heat transfer through conduction and convection to the expander. The first stage of the expander system provides active cooling to the radiation shield, which protects the second stage from room temperature thermal radiation that the vacuum shroud emits [41].

Figure 2.5: Typical closed cycle cryostat including radiation shield, vacuum shroud, cold head, compressor, and hoses [41].

The refrigeration system operates through a four-stage process, which begins with High-Pressure Intake when a rotating valve disk permits high-pressure helium gas to enter the regenerator and proceed into the expansion area. The Expansion phase produces a pressure differential that forces the displacer upward, which allows gas to expand into the increasing volume while it cools down. The Low-Pressure Exhaust stage starts when the valve disk rotates to create a low-pressure opening, which compels cold gas to flow back

through the regenerator for system heat removal. The Cycle Completion phase begins when the pressure differential returns the displacer to its original position, which prepares the system for its next intake operation [41].

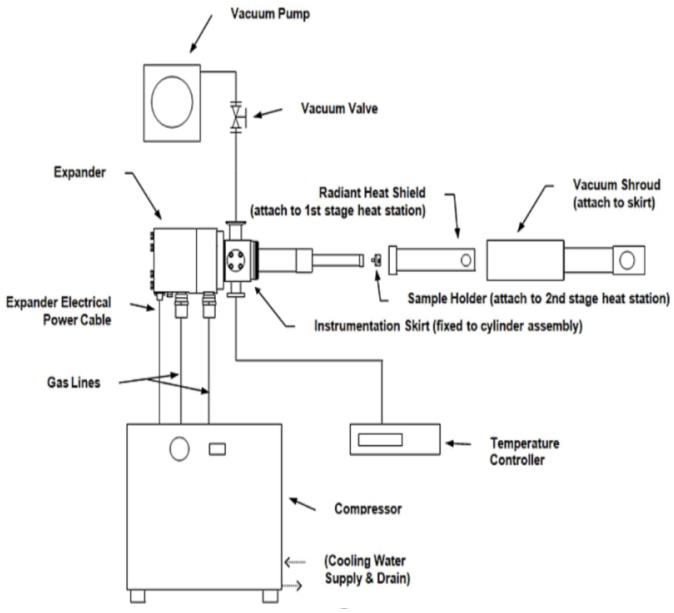

Figure 2.6: Structural overview of the cryostat assembly. [41].

The CCR setup uses Silicon (Si) Diodes and Cernox™ (Thin-Film Resistance) sensors for temperature measurement. Silicon diodes are highly favored for their high sensitivity and remarkably linear voltage-temperature response across a broad range, typically from 1.4 K to 500 K. The Cernox™ sensors that use zirconium-oxynitride thin film material are used for specialized applications. The system displays unique features because it maintains high stability while also producing minimal magnetic fields induced errors, making it ideal for testing in environments that need precise temperature measurement for minor temperature changes (ΔT) [42].

The strategic sensor placement at two points inside the cryostat enables precise thermal measurement throughout the system. The control sensor, which is Si diode for the temperature controller system, requires it to be securely fixed at either the cryotip or coldhead. The Cernox™ sensor, which has greater sensitivity, has to be installed on the sample or its mounting substrate. The dual-sensor system enables complete temperature measurement of the sample while detecting thermal differences between the cooling source and the test specimen during quick temperature changes and intense optical power testing.

2.4.1 Resistance Measurement

The electrical characterization of the pellet was performed through resistivity measurements, which were conducted within a Closed Cycle Refrigerator (CCR) operating. The primary measurement system of the experiment used a Keithley 6221 DC/AC Current Source together with a Keithley 2182A Nanovoltmeter, which functioned in a four-probe measurement system, and this setup eliminates lead and contact resistance errors. To achieve total data reliability and testing reproducibility, a Keithley 2450 SourceMeter was used to independently verify current-voltage (I-V) characteristics (for R-T measurement verification only).

The Lakeshore 360 Temperature Controller system regulates temperature through its PID algorithm, which provides stable temperature control. A Cernox™ sensor, which operates between 4 K to 325 K, was installed on the sample holder to measure the thermal condition of the sample. The proper wiring thermal anchoring system keeps the sample warm by blocking any heat transfer to the surrounding environment.

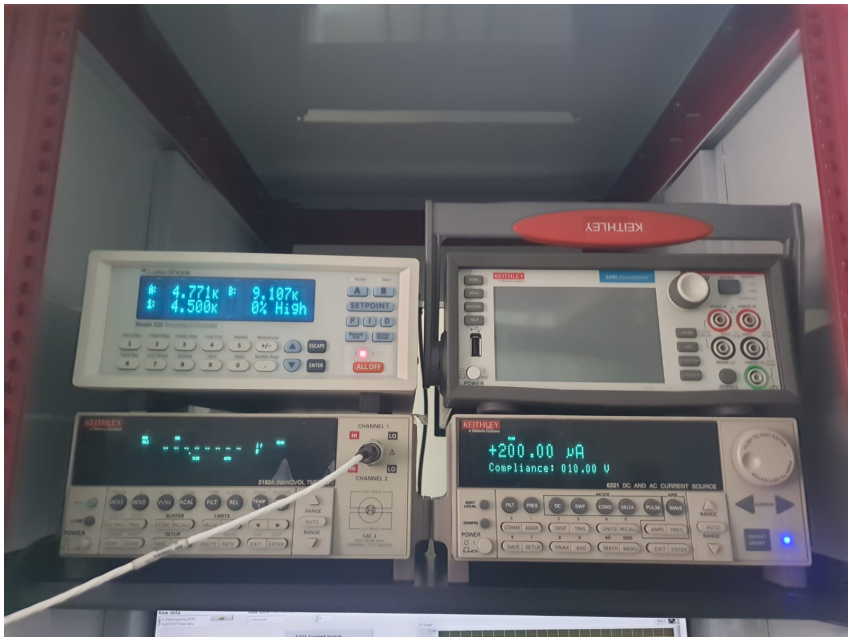

Figure 2.7: Instrumentation setup for electrical characterization including, Lakeshore 336 temperature controller and a Keithley measuring unit.

Chapter 3

Characterization of Fe_2O_3@CNT Composite

This chapter presents a comprehensive investigation of the structural, morphological, and vibrational properties of the Fe_2O_3@CNT composite pellet. The sample was characterized using X-ray diffraction, Raman Spectroscopy, and Scanning Electron Microscopy to confirm the hybrid system's morphology, structural integrity, and phase composition before beginning the transport measurements. The analyses demonstrate how the successful integration of iron oxide with carbon nanotubes was achieved, and they create the foundation for future electrical transport research. This study made use of Fe_2O_3@CNT sample that was synthesized by Dr Aparna C and D. Hima bindhu and subsequently used for structural characterization and transport measurements.

3.1 X-ray Diffraction (XRD)

The XRD pattern displays multiple sharp diffraction peaks, which establish the crystalline structure of the sample. The prominent peaks observed at $2\theta \approx 24°$, 33°, 35.6°, 40.8°, 49.4°, 54°, 62.4° and 64.1° can be indexed to the (012), (104), (110), (113), (024), (116), (214), and (300) planes of rhombohedral α-Fe_2O_3 (hematite), indicating that hematite is the dominant phase in the composite [56, 57]. The diffraction peak which occurs at $2\theta \approx 57.6°$ shows primary characteristics of hematite (α-Fe_2O_3) through its specific reflections which can be indexed to rhombohedral structure planes (018) and (122). However, the presence of a peak in this region may also indicate contributions from spinel-type iron oxide phases, such as γ-Fe_2O_3 (maghemite) or Fe_3O_4 (magnetite), where reflections like the (511) plane occur near similar 2θ values. The peak indicates that dominant hematite formation occurred together with a minor presence of secondary iron oxide phases.

A characteristic broad peak around $2\theta \approx 26°$ corresponds to the (002) plane of graphitic carbon, confirming the presence of multi-walled carbon nanotubes (MWCNTs). The peak shows broad characteristics because it displays turbostratic or partially disordered graphitic layers, which occur in CNT networks [56, 58].

In addition, a distinct peak which occurs at $2\theta \approx 44.8°$ originates from the (110) plane of metallic iron and demonstrates that the sample contains a minor amount of unoxidized iron, suggesting that the process of converting Fe to Fe_2O_3 during synthesis has not achieved complete conversion [58].

The XRD results provide evidence that three materials, α-Fe_2O_3, CNTs, and trace metallic Fe, exist together in the hybrid structure, which affects charge transport and interfacial interactions.

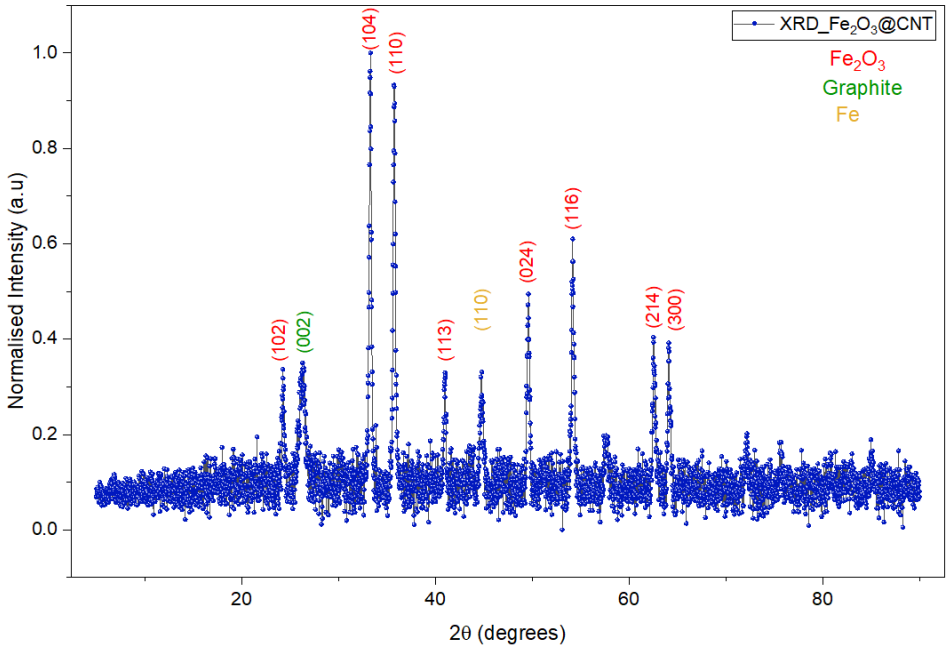

Figure 3.1: X-ray diffraction pattern of Fe_2O_3@CNT composite showing characteristic peaks of both α-Fe_2O_3 and carbon nanotubes.

3.2 Raman Spectroscopy

The spectrum displays a prominent G-band of peaks at approximately 1579 cm^{-1}, resulting from the in-plane stretching mode that occurs with E_{2g} symmetry of sp^2-bonded carbon atoms, which represents graphitic ordering [55]. A distinct D-band is present at approximately 1344 cm^{-1}, arising from disorder-induced scattering because of defects, finite size effects, and structural distortions in the CNT walls. The presence of a well-defined 2D (G') band around 2696 cm^{-1} further confirms the graphitic structure and long-range ordering of the CNT shells [54, 55].

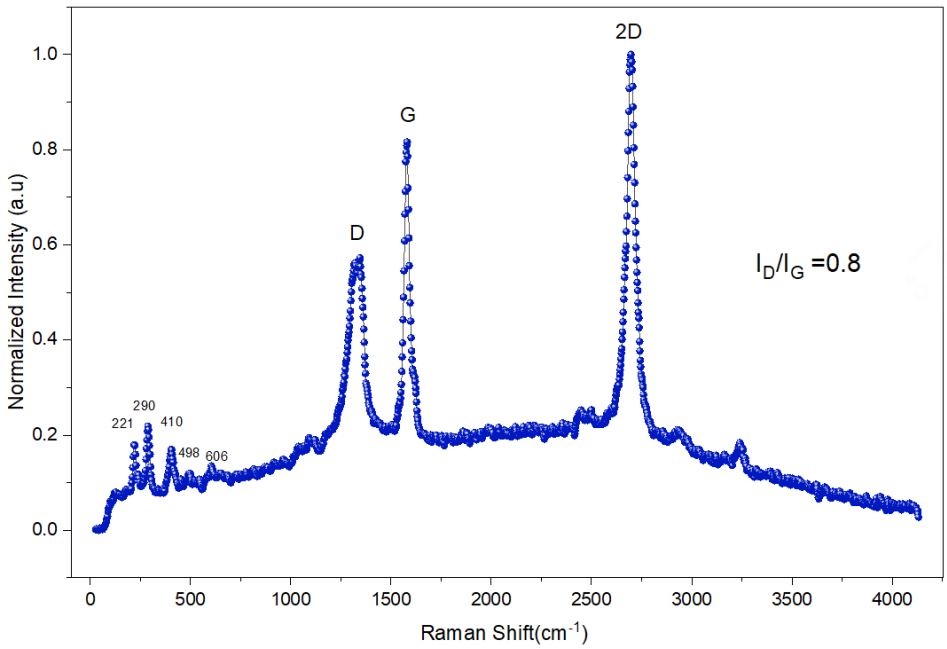

Figure 3.2: Raman spectrum of Fe_2O_3@CNT composite shows the characteristic G-band, D-band, and 2D-band of carbon nanotubes along with Raman-active modes of α-Fe_2O_3.

The intensity ratio of the D-band to the G-band (I_D/I_G) in Raman spectroscopy serves as a standard measurement that is used to determine the level of structural disorder and graphitization present in carbon nanotubes. The D-band intensity in pristine single-walled carbon nanotubes (SWCNTs) shows an extremely low value (< 0.1) because of their high structural symmetry, resulting in nearly negligible D-band [61]. The I_D/I_G ratio of multi-walled carbon nanotubes (MWCNTs) shows higher values, which range from about 0.5 to 1.5 because these nanotubes possess multiple concentric walls and inherent structural imperfections [62].

The I_D/I_G ratio increases because the system experiences greater disorder when its D-band intensity rises through defect-based scattering while its G-band strength decreases. This behaviour suggests that sp^3 defects increased while crystallite size decreased and the material progressed towards more disordered or amorphous carbon state.

The intensity ratio I_D/I_G, which has a value of approximately 0.8, shows that the CNT network contains a moderate amount of disorder. The graphitic structure mostly remains intact, but the addition of Fe_2O_3 together with interfacial strain effects creates defects in the CNT framework.

The Raman-active modes of α-Fe_2O_3, which show two A_{1g} and five E_g vibrations, display their weak features below $1000\,cm^{-1}$. The A_{1g} modes appear at approximately $221\,cm^{-1}$ and $498\,cm^{-1}$, while E_g modes emerge at approximately $244\,cm^{-1}$, $293\,cm^{-1}$, $412\,cm^{-1}$, and $609\,cm^{-1}$ which result from Fe-O lattice vibrations [56]. The Fe_2O_3@CNT

composite shows peak distribution below 1000 cm^{-1} because of nanoscale effects and CNT signal dominance, which shows the existence of strong interfacial connections.

3.3 Scanning Electron Microscopy (SEM)

The SEM micrographs of the Fe_2O_3@CNT composite at different magnifications show a hierarchical multi-scale structure that combines carbon nanotube (CNT) networks with iron oxide.

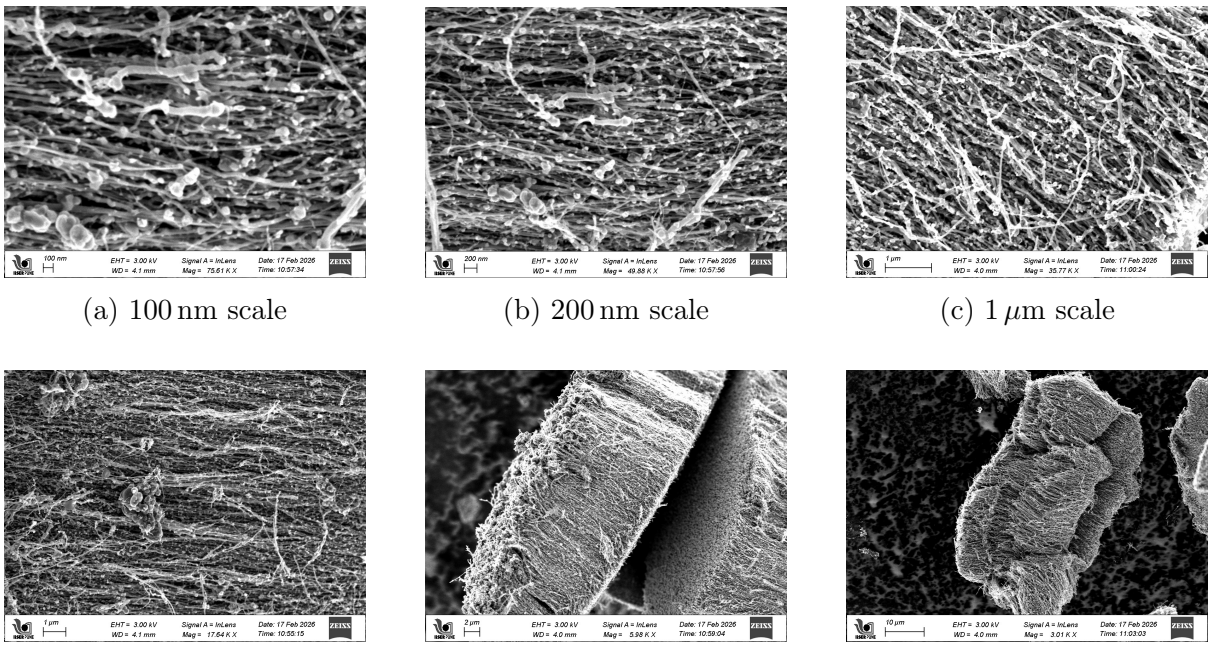

(a) 100 nm scale (b) 200 nm scale (c) 1 μm scale

(d) 1 μm scale (e) 2 μm scale (f) 10 μm scale

Figure 3.3: FESEM micrographs of Fe_2O_3@CNT composite at different magnifications showing the surface morphology and structural features.

At higher magnifications (100–200 nm scale, Fig. 3.3a–3.3b), a dense and entangled network of CNTs is observed. The nanotubes appear as elongated, fibrous structures which create a continuous web-like architecture. The presence of small particulate features which attach along the CNT surfaces shows that Fe_2O_3 nanoparticles have deposited there and it demonstrates strong interfacial interaction between the oxide and the nanotube framework.

At intermediate magnifications (1 μm scale, Fig. 3.3c–3.3d), the CNT network shows multiple conductive paths which connect through various nanotubes that extend across different sections. The interconnected morphology of the material establishes essential pathways which enable electrical charges to move through the composite. The distribution appears relatively uniform, although some localized agglomeration is present.

The lower magnification level of 2 and 10 μm (Fig. 3.3e–3.3f) shows larger Fe_2O_3 particles with rough and irregular surfaces, which function as a structural foundation

that supports the wrapping of CNTs. This rough morphology enhances CNT anchoring and interfacial contact.

In general, the images prove a well-interconnected multi-scale structure that fosters electrical transportation.

Chapter 4

Electrical Transport Measurements

The chapter presents the process of preparing Fe_2O_3@CNT pellet and describes the methods used to measure their electrical conductivity as a function of temperature. Measurements are done using a four-probe method using a Closed Cycle Refrigerator (CCR) system, which is explained in this section. The study serves as the foundation for the upcoming research on the fundamental nature of transport mechanisms and the use of such composites as magnetoresistive sensors.

4.1 Sample Integration

The synthesized Fe_2O_3@CNT nanocomposite powder was compressed using a 6 mm stainless steel die set. The powder was loaded into the die set, which underwent uniaxial hydraulic pressing that applied a few tons of pressure to produce a dense, mechanically stable pellet that maintained uniform thickness throughout. The chosen diameter offers enough surface area, which allows four-probe leads to operate without crowding, while still providing a compact design that fits securely onto a sapphire glass plate.

The pressed pellet was mounted on a sapphire plate using GE varnish. Sapphire serves as the substrate because it possesses two crucial properties: the material functions as an electrical insulator, which prevents cryostat body leakage currents, and it exhibits outstanding thermal conductivity. The GE Varnish functions as a cryogenic adhesive that maintains its stability throughout the complete temperature spectrum from 4 K to 300 K. GE varnish is a good electrical insulator and a good thermal conductor. It can maintains strong thermal connections between the pellet and sapphire material.

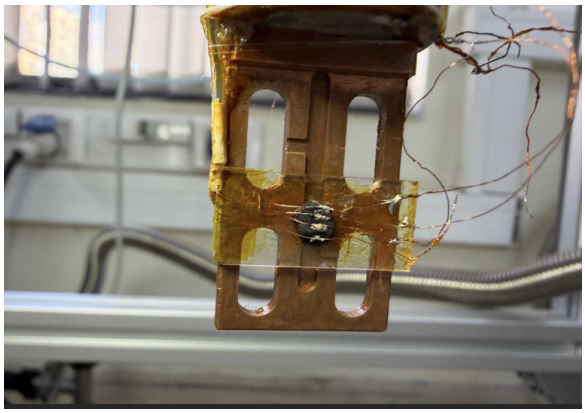

(a) Sample placement

(b) Cernox™ placement

Figure 4.1: The sample mounting assembly, showing the hybrid pellet and the thermal anchoring of the Cernox™ sensor.

The electrical connection to the Fe_2O_3@CNT pellet was established through the high-precision four-probe method, which ensures the accuracy of transport measurements. The four copper leads were placed on the top surface of the pressed pellet. The leads were attached to the sample through high-purity silver conductive paste, ensuring each contact point is discrete and isolated. Silver paste was selected because of its superior electrical conductivity and its capability to sustain mechanical bonds at cryogenic temperatures. The two outer leads were designated for current sourcing ($I+$ and $I-$), while the two inner leads were reserved for measuring the longitudinal voltage drop ($V+$ and $V-$). The use of silver paste enabled us to establish a low-resistance ohmic contact, which plays a vital role in reducing contact resistance that frequently affects transition metal oxide measurements.

This Sapphire-pellet assembly was then securely fixed to the OFHC (Oxygen-Free High Conductivity) copper sample holder of the CCR using varnish. This anchoring ensures that the temperature of the pellet is in equilibrium with the Cernox™ sensor, maintaining minimum thermal lag.

The correspondence between the inner CCR wires (connected to the Fe_2O_3@CNT pellet) and the outside cord wires (connected to the Keithley instruments) was verified using a continuity test with a digital multimeter. Upon securing the leads to the sample, the ends of these four wires were soldered directly to the inner cryostat wiring. In addition to continuity, the wires were checked against each other and the cryostat body to ensure no short circuits existed.

4.2 Room Temperature I-V Characteristics

The first step of electrical characterization started with testing the current-voltage (I-V) behavior of the Fe_2O_3@CNT nanocomposite at room temperature (300 K). This step is essential for verifying ohmic contact.

The characterization used two separate setups to validate the accuracy of transport measurements. The first setup used is the Keithley 2450 SourceMeter, which utilizes Force HI and Force LO for current measurement and Sense HI and Sense LO for four-wire voltage drop assessment. The second setup combined a Keithley 6221 Current Source with a 2182A Nanovoltmeter. The 6221/2182A system functions as a dedicated solution that performs precise low-level measurement tasks. The 2182A Nanovoltmeter delivers a superior noise floor and better resolution than the 2450 SourceMeter.

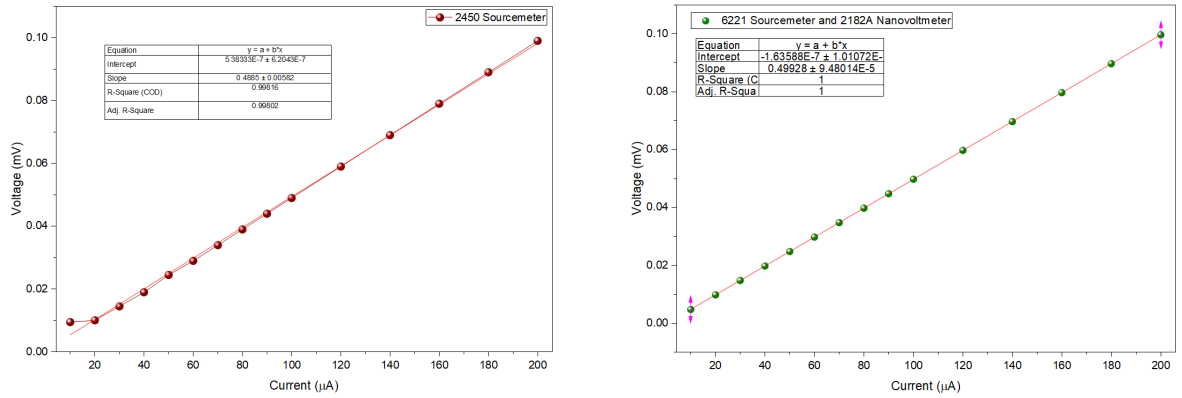

(a) Keithley 2450 I-V Curve

(b) Keithley 6221/2182A I-V Curve

Figure 4.2: Current-Voltage (I-V) characteristics of Fe_2O_3@CNT pellet at room temperature measured using (a) Keithley 2450 SourceMeter and (b) Keithley 6221/2182A system.

The I-V curves shown in Figure 4.2 demonstrate that the 2450 SourceMeter data showed visible noise-induced fluctuations at the base point during the low-current range, and the Keithley 6221/2182A system gave better resolution than the 2450 instrument, which has higher voltage noise levels. Therefore, high priority was given to the 6221/2182A setup to deliver data with the highest integrity for temperature-dependent studies to follow.

Overall, the current-voltage (I-V) characteristics obtained from both instrumentation setups demonstrated a high degree of linearity across the entire measured range ($-200\,\mu$A to $200\,\mu$A). The widespread linearity of the measurements proves that the Fe_2O_3@CNT pellet displays Ohmic transport behavior at room temperature, implying no grain boundaries or contact barriers. The I-V relationship slope calculation allowed us to determine resistance values, which we used to compare consistency between both systems. The Keithley 2450 measured resistance at approximately 0.48 Ω while the Keithley 6221/2182A combination produced a more accurate measurement of 0.49 Ω.

4.3 Temperature-Dependent Transport Analysis

After validating the system at room temperature, the pellet was subjected to automated temperature-dependent measurement within the Closed Cycle Refrigerator (CCR). We used a custom LabVIEW-based automation program to acquire data, which enables us to take automated data. The temperature step size of 0.5 K was used throughout the temperature range of 5 K to 300 K.

The experimental procedure required multiple thermal sweeps to verify that the electronic states of the Fe_2O_3@CNT nanocomposite would produce identical results under different thermal conditions. We started the initial cooling tests by using relatively low currents of 50 μA and 100 μA, which served as baseline measurements to determine the resistance of the pellet. Subsequent heating and cooling cycles were conducted at higher current densities of 200 μA and 500 μA to see the current dependence, especially around the Morin Transition temperature and improve the signal-to-noise ratio.

The resistance (R) versus temperature (T) plots, which were produced at different currents, show a typical semiconducting behavior because they show a negative temperature coefficient of resistance ($dR/dT < 0$), which will be discussed in the next chapter.

Chapter 5

Results and Discussion

This chapter presents the temperature-dependent electrical transport behavior of the Fe_2O_3@CNT composite over the temperature range of 5 K to 300 K. The resistance measurements are analyzed to examine the overall conduction characteristics of the system.

The study includes measurements under different bias currents during both heating and cooling cycles to probe possible variations in transport behavior. Standard analysis methods were employed, which included Arrhenius and Variable Range Hopping (VRH) models, to investigate the conduction mechanisms. The results are discussed in the context of the structural and interfacial features of the composite material.

5.1 General Characteristics and the Baseline Trend

The electronic transport properties of iron oxide-filled carbon nanotubes Fe_2O_3@CNT are characterized by an intricate interplay between the magnetic state of the encapsulated material and the electrical properties of the outer graphitic shells. The Resistance vs. Temperature (R vs. T) plots for the sample Fe_2O_3@CNT show an overall semiconducting behavior. In addition, anomalies in the vicinity of the expected Morin transition of the encapsulate are also observed in the temperature variation of the resistivity. The resistance (R) grows steadily as the temperature (T) drops from 300 K to 5 K.

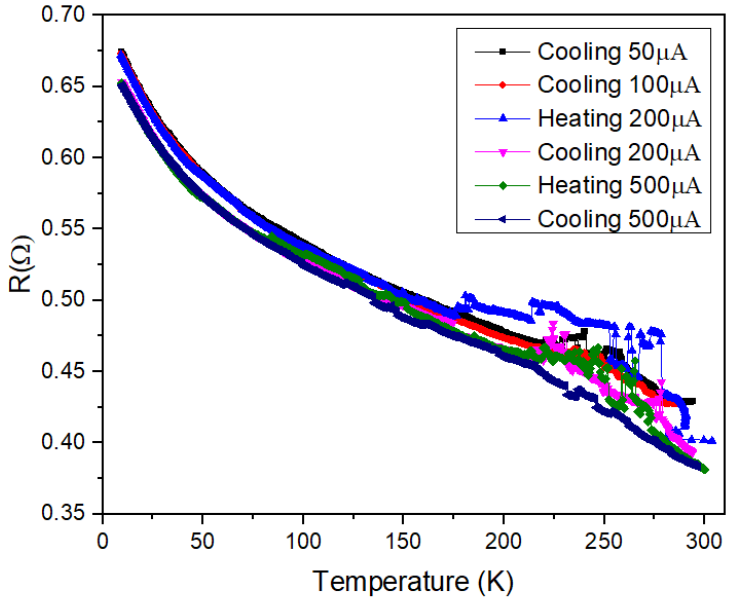

Figure 5.1: Overall Resistance vs. Temperature plot for Fe_2O_3@CNT from 5 K to 300 K showing the baseline semiconducting behavior

5.2 The Morin Transition Region

As is evident from Fig. 5.1, anomalies in resistance vs. temperature data are observed in the temperature region between 150 K to 300 K.This region coincides with the Morin transition temperature (T_M) of α-Fe_2O_3; T_M exists at approximately 260 K in bulk Fe_2O_3, and it is observed to decrease to lower temperatures in nanowire and nanoparticle states because of nanoscaling effects [45, 46]. This appears as a fundamental property of the hybrid structure through this robust anomaly, which exists at all tested bias currents of 50 μA, 100 μA, 200 μA, and 500 μA rather than experimental noise. More importantly, heating and cooling cycles (while keeping the same current) also show thermal hysteresis in the vicinity of the Morin transition.

5.2.1 Interfacial Effects on Transport Behavior

The anomalous transport that was observed can be correlated with the spin reorientation transition of the hematite (α-Fe_2O_3) core. Hematite is a room-temperature antiferromagnet that undergoes spin-reorientation at T_M. Below T_M, the magnetic spins align themselves in parallel orientation with the crystallographic c-axis, which leads to the formation of a pure antiferromagnetic (AFM) state. Above T_M, the spins change their orientation to the basal plane while they develop spontaneous spin canting that results from the Dzyaloshinskii-Moriya Interaction (DMI). The canting establishes a weak ferromagnetic (WFM) moment in an otherwise antiferromagnet. The sudden shift in internal

magnetic symmetry, together with the onset of weak ferromagnetism, causes disruption to the electronic scattering processes that occur in the surrounding CNT shells; especially significant strain effects in the graphitic shells of CNT are observed in the vicinity of the Morin Transition. These strain effects are observed in the lattice parameters of CNT obtained through temperature variation of synchrotron XRD data [46].

The transport behavior evidence shows that the Fe_2O_3 core can significantly affect transport through strain effects transmitted through the interface between the oxide encapsulant and the CNT. Previous studies have reported that interfacial strain and spin-related effects can influence the coupling between magnetic oxides and graphitic systems [46]. The Morin transition temperature is known to cause strain in carbon nanotubes, such as lattice parameter "a" undergoing major strain effects at about 250 K, which precisely matches the Morin transition temperature of α-Fe_2O_3 as reported by Kapoor et al. [46]. The interfacial effects between carbon nanotubes and the composite materials affect their electrical charge transport because carbon nanotubes show extreme sensitivity to both lattice distortions and external disturbances [47]. The transition region shows resistance fluctuations, which we believe occurs because of strain-based changes and electron scattering variations that happen at the Fe_2O_3–CNT interface. The graphitic interface experiences physical stress from the magnetic reorientation process, which can change the electronic pathway of the nanotube and produces irregular patterns in the R vs. T graph showing macroscopic evidence of a microscopic magnetic phase transition. Data at closer intervals in different samples would be needed to further confirm this. Our understanding of these mechanisms needs additional research through experimental work.

5.3 Thermal Hysteresis and Asymmetric Fluctuations

The transport data from the Morin transition region shows a unique thermal hysteresis pattern which exhibits different temperature pathways during its heating and cooling cycle. The first-order nature of the magnetic phase transition in Fe_2O_3 causes this system to follow specific path-dependent behavior. First-order transitions are characterized by a discrete jump in the order parameter and the existence of thermal hysteresis, meaning the system follows different paths during heating and cooling cycles [48, 49].

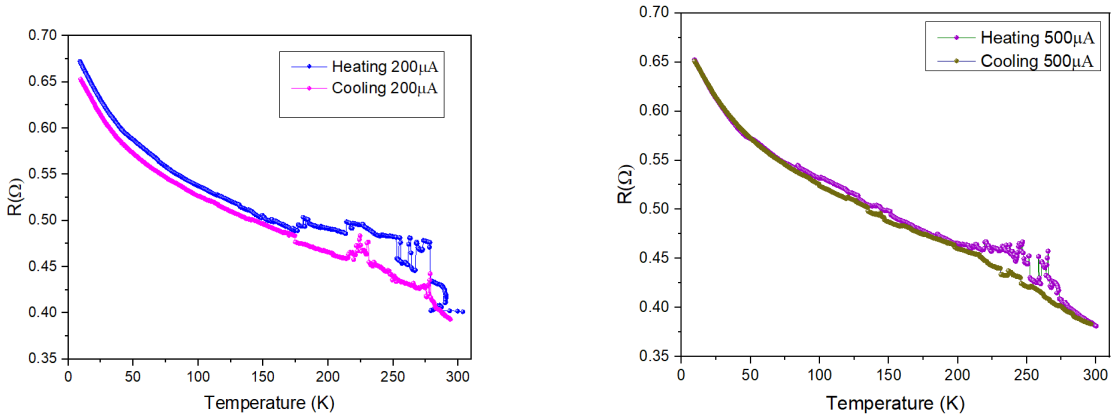

(a) 200 μA bias current

(b) 500 μA bias current

Figure 5.2: Resistance vs. Temperature plots at different bias currents showing different heating and cooling branches with characteristic resistance fluctuations.

The experimental plots show that the heating branch between 200 K and 300 K demonstrates more unstable than the cooling branch. The system needs to transform from its complete antiferromagnetic (AFM) state into a partially ferromagnetic (WFM) state driven by spontaneous spin canting as the temperature rises to approach T_M. This reorganization involves the nucleation and growth of new magnetic domains, creating a state of phase coexistence that is inherently noisy [46, 48]. The signal exhibits significant noise when approaching the transition temperature because of thermal fluctuations that accompany the phase change. The system experiences its most extreme fluctuations during the heating process, which leads to the breakdown of its low-temperature magnetic order as it transitions into the canted state.

Furthermore, the heating process is characterized by physical shocks at the interface. The sudden structural jumps, which occur during the heating process when the core's lattice structure expands to accommodate the new magnetic state, create interfacial strain on the carbon nanotube shells [46]. The lattice shocks that occur during the transition process create jagged resistance spikes that appear in the heating curves because carbon nanotubes react excessively to physical disturbances and strain. At this point, it is not clear why heating data is more noisy than cooling data. However our experiments show that such a pattern is repeatedly seen, at least for this particular sample. To further confirm this, we need more measurements in well-formed pellets.

5.4 Impact of Bias Current on Electronic Transport and Transition Dynamics

The bias current in the investigation of iron oxide-encapsulated carbon nanotubes serves as more than just a measurement parameter; it functions as a dynamic probe that seems

to control the hybrid system's response to the core's internal magnetic phase transition. The Resistance vs. Temperature (R vs T) at 200 μA and 500 μA reveal distinct shifts and character of Morin transition.

We observe that the window of thermal hysteresis between heating and cooling cycles reduces when R vs T is recorded at higher currents. These data indicate that I-V isotherms in the low, intermediate, and high temperature regions are needed.

5.5 Transport Model Analysis

The temperature-dependent resistance data was analyzed using standard transport models to gain insight into the conduction mechanism for these hybrids. The Arrhenius model and the Variable Range are well known for understanding conductivity mechanisms, particularly the oxide-based semiconductors.

Before fitting the model, the temperature-dependent resistance data was converted to electrical conductivity for analysis with standard transport models. The electrical conductivity (σ) is related to resistance (R) through the sample geometry as:

$$\sigma = \frac{L}{R \cdot A} \tag{5.1}$$

where L is the distance between voltage probes and A is the cross-sectional area of the pellet. For the present sample, $L = 1.18\,\text{mm}$, while the cross-sectional area was calculated using the measured width and thickness of the pellet, where the width and thickness were measured to be 3.16 mm and 0.9 mm, respectively.

Using these dimensions, a constant geometrical factor (L/A) was obtained, allowing conductivity to be expressed as:

$$\sigma(T) = \frac{G}{R(T)} \tag{5.2}$$

where G is the geometry-dependent constant. This conversion was applied to all resistance data points prior to performing transport model analysis.

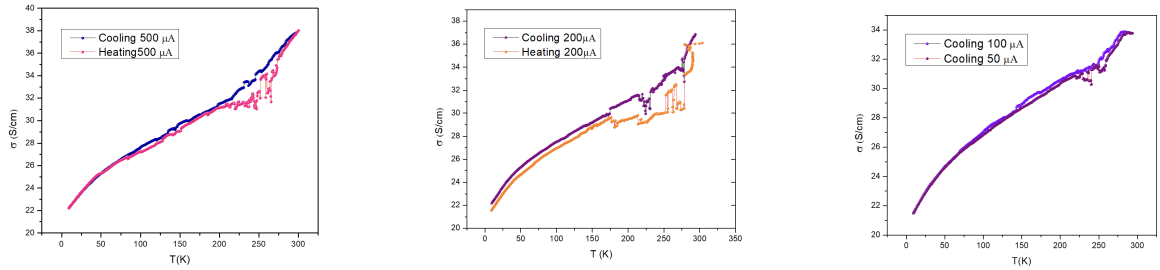

(a) 500μA (b) 200μA (c) Low-current regimes

Figure 5.3: Temperature-dependent electrical conductivity (σ) plots for the Fe_2O_3@CNT hybrid under varying bias currents.

5.5.1 The Arrhenius Model

The transport of charge carriers in solid-state materials is often governed by thermally activated processes which operate as the main mechanism for charge transport in semiconductors and transition metal oxides. The electrical conductivity (σ) of these systems exhibits an Arrhenius-type relationship, which shows that conduction increases with temperature according to an exponential function [58, 59].

$$\sigma(T) = \sigma_0 \exp\left(-\frac{E_a}{k_B T}\right) \tag{5.3}$$

Taking the natural logarithm:

$$\ln \sigma = \ln \sigma_0 - \frac{E_a}{k_B} \cdot \frac{1}{T} \tag{5.4}$$

Thus, a plot of $\ln \sigma$ versus $1/T$ should yield a straight line with slope:

$$\text{slope} = -\frac{E_a}{k_B} \tag{5.5}$$

where E_a represents the activation energy required for charge transport. A linear dependence of $\ln(\sigma)$ on $1/T$ is expected if the conduction mechanism is dominated by thermally activated processes.

The charge transport mechanism in Fe_2O_3 materials operates through the thermally activated hopping movement of localized charge carriers often associated with lattice distortion and disorder. This behavior has been widely reported in pure hematite, where conduction occurs via small polaron hopping between Fe^{2+}/Fe^{3+} sites [60]. The composite system Fe_2O_3@CNT can exhibit complex behavior because it contains both conductive carbon nanotube pathways and insulating oxide residing inside the core cavity of CNT, which can create multiple transport pathways together with interfacial transport phenomena.

Therefore, the Arrhenius model serves as a first approximation for studying thermally

activated conduction.

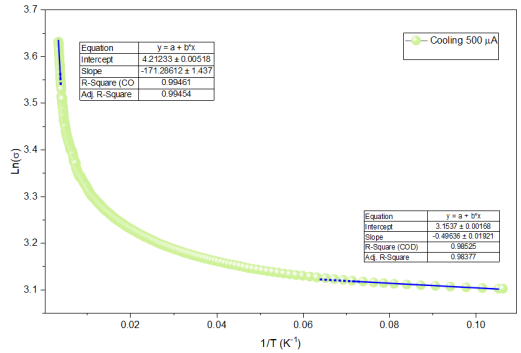

(a) Cooling Profile

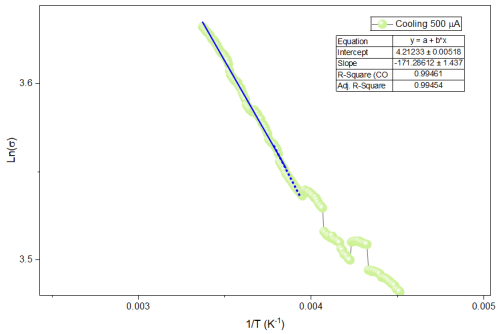

(b) Magnified view of the high-temperature region during cooling.

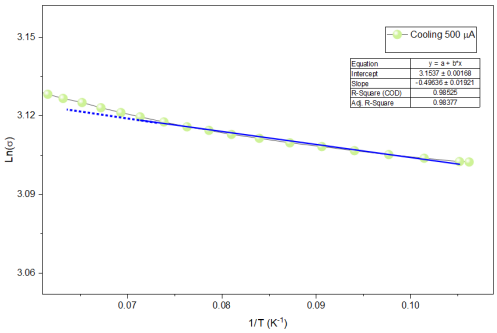

(c) Magnified view of the low-temperature region during cooling.

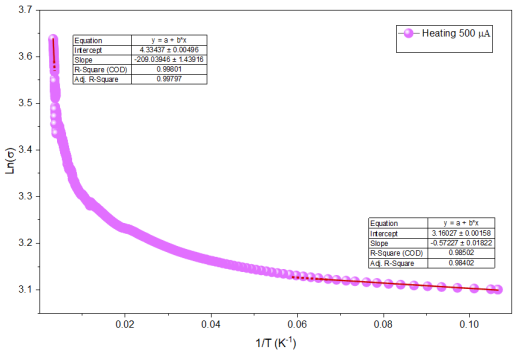

(d) Heating Profile

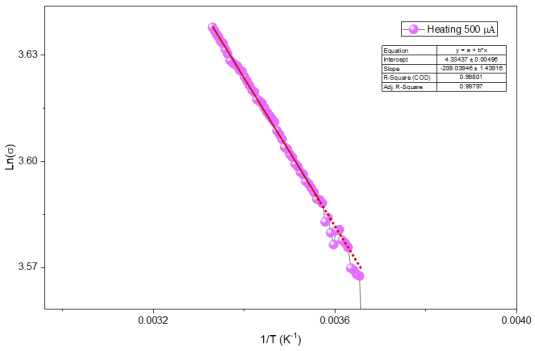

(e) Magnified view of the high-temperature heating regime.

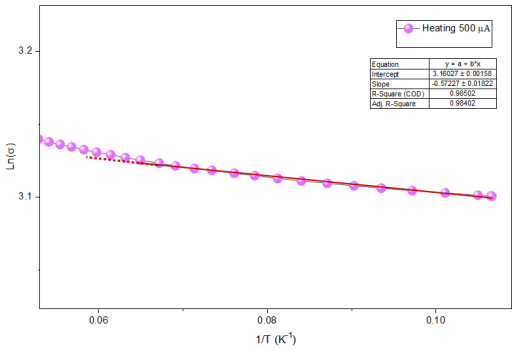

(f) Magnified view of the low-temperature heating data

Figure 5.4: Comparative $\ln(\sigma)$ vs. $1/T$ plots for (a–c) cooling and (d–f) heating at 500 μA, highlighting the deviation from ideal linear Arrhenius behavior.

The Arrhenius fitting was performed for both the low and high temperature regions using the 500 μA heating and cooling datasets. The $\ln(\sigma)$ versus $1/T$ plots show approximate linear behavior in a very small temperature window, which usually indicates thermally activated conduction. The temperature regimes show clear deviations from

linearity, which become most evident when temperature data is analyzed closely.

From the linear fitting of the experimental data (Fig. 5.4a), the slope values were extracted for different temperature regions. Using the relation:

$$E_a = -(\text{slope}) \times k_B \tag{5.6}$$

where $k_B = 8.617 \times 10^{-5}$ eV/K,

High-temperature region:

$$\begin{aligned} \text{slope} &\approx -171.286 \\ E_a &= 171.286 \times 8.617 \times 10^{-5} \\ &\approx 0.0148 \text{ eV} \end{aligned}$$

For an intrinsic semiconductor, conductivity is given by:

$$\sigma(T) \propto \exp\left(-\frac{E_g}{2k_B T}\right) \tag{5.7}$$

where E_g is the band gap energy.

$$E_g = -2 \times (\text{slope}) \times k_B \tag{5.8}$$

$$\begin{aligned} \text{slope} &\approx -171.286 \\ E_a &= 2 \times 171.286 \times 8.617 \times 10^{-5} \\ &\approx 0.0296 \text{ eV} \end{aligned}$$

The obtained energies are relatively small, which indicates that charge transport does not occur through a simple band-like mechanism. The values suggest that conduction can occur through hopping processes that connect different localized states.

The small value of E_a and E_g, along with the non-ideal linearity, supports disorder-induced transport mechanisms and electronic heterogeneity. The presence of conductive CNT pathways together with disordered oxide regions creates localized states which develop potential barriers, thus enabling carrier transport through hopping or tunneling mechanisms instead of the band-like conduction method. Oxide semiconductors are known to exhibit such crossover regions.

5.5.2 Variable Range Hopping (VRH)

The Fe_2O_3@CNT system can enter a localized transport state with the possibility of hopping of charge carriers between different sites that provide low energy levels. The

process, according to Mott, proceeds through Variable Range Hopping (VRH) as its controlling mechanism. This model of conduction explains conduction at low temperatures in strongly disordered systems characterized by the presence of localized states [50].

The general temperature dependence of conductivity (σ) in disordered systems is represented as:

$$\sigma(T) = \sigma_0 \exp\left[-\left(\frac{T_0}{T}\right)^{\alpha}\right] \tag{5.9}$$

Since we measure resistance R and $\sigma \propto 1/R$, we get:

$$R(T) = R_0 \exp\left[\left(\frac{T_0}{T}\right)^{\alpha}\right] \tag{5.10}$$

The equation becomes linear after we apply the natural logarithm function which results in this formula for data fitting purposes:

$$\ln(R) = \ln(R_0) + \left(\frac{T_0}{T}\right)^{\alpha} \tag{5.11}$$

The exponent, defined as $\alpha = 1/(1+d)$, is a crucial parameter that defines the character of hopping and the dimensionality d of the system. T_0 indicates the Mott characteristic temperature, which indicates the degree of disorder and is inversely proportional to the localization length (a) and the density of states $N(E_F)$, which is approximately given by:

$$T_0 \approx \frac{18}{a^3 N(E_F) k_B}; \qquad N(E_F) = \frac{18}{a^3 k_B T_0} \tag{5.12}$$

[50]

Mott-VRH (M-VRH): It happens when the density of states $N(E_F)$ is constant near the Fermi level [50].

- **3D M-VRH ($\alpha = 1/4$):** Typical for bulk disordered semiconductors.
- **2D M-VRH ($\alpha = 1/3$):** The behavior typically occurs in thin films, layered materials, and in systems that have conductive pathways that exist only at their flat surfaces.
- **1D M-VRH ($\alpha = 1/2$):** Often observed in individual Carbon Nanotubes or quasi-1D polymer chains [50].

Efros-Shklovskii VRH (ES-VRH): Long-ranged electron-electron interactions lead to a Coulomb-induced gap up at the Fermi energy. Here, $\alpha = 1/2$, regardless of the dimensionality [50].

The literature [51–53] shows that a crossover from Mott ($\alpha = 1/4$) to ES-VRH ($\alpha = 1/2$) occurs when the temperature decreases. The hopping energy exceeds the Coulomb

gap at high temperatures, which results in Mott's model being the preferred explanation. The system usually transitions into ES-VRH behavior because the Coulomb interaction becomes the main force at lower temperatures. Our hybrid system uses CNTs, which function as 1D conducting pathways, whereas Fe_2O_3 serves as a disordered matrix. The CNT concentration, together with temperature changes, can lead to different transport dimensions [50].

The analysis was performed on both heating and cooling cycles at a bias current of $500\,\mu$A. This is shown in Fig. 5.5 and Fig. 5.6. The data was fitted with various values of α, corresponding to various dimension-dependent VRH models. However, as is evident from Fig. 5.5 and Fig. 5.6, similar to the Arrhenius case, there is no reasonable linear region or crossover phenomenon. Nevertheless, from the linear region in the intermediate temperature range shown in Fig. 5.5e, we attempted to estimate parameters such as T_0. This did not lead to a reasonable value, typically observed in oxide-based semiconductors. The Mott 3D Variable Range Hopping (VRH) conductivity is given by:

$$\sigma = \sigma_0 \exp\left[-\left(\frac{T_0}{T}\right)^{1/4}\right] \tag{5.13}$$

Taking the natural logarithm:

$$\ln\sigma = \ln\sigma_0 - \left(\frac{T_0}{T}\right)^{1/4} \tag{5.14}$$

Thus, a plot of $\ln\sigma$ versus $T^{-1/4}$ should yield a straight line, where the slope is related to the Mott characteristic temperature T_0 as:

$$\text{slope} = -T_0^{1/4} \tag{5.15}$$

Calculation of T_0

From the linear fit of the experimental data (Fig. 5.5e), the slope was obtained as:

$$\text{slope} \approx -1.15779 \tag{5.16}$$

Therefore,

$$T_0^{1/4} = 1.15779 \tag{5.17}$$

Raising both sides to the power of 4:

$$T_0 = (1.15779)^4 \approx 1.8 \text{ K} \tag{5.18}$$

The low value of T_0 demonstrates weak localization because the presence of a conductive CNT network improves charge transport by extending the effective localization length.

The linear fitting method maintains its validity only within a specific temperature range. The extracted value of T_0 should be treated as an estimated parameter that shows hopping-based transport, instead of serving as a complete explanation of the conduction process.

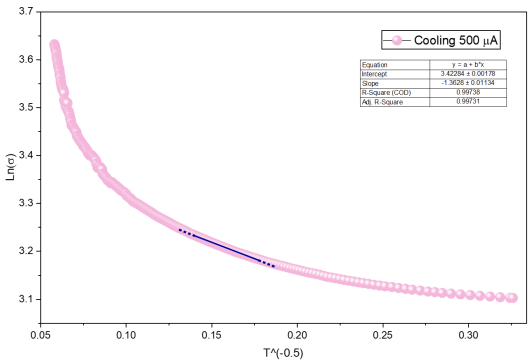

(a) 1D VRH

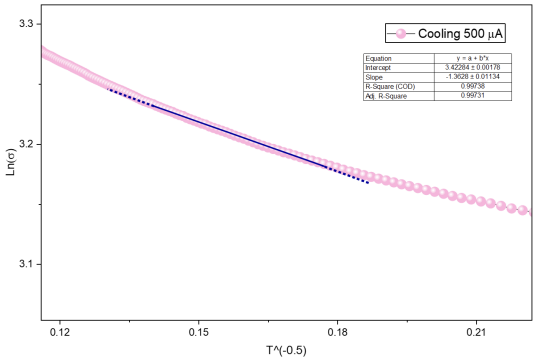

(b) 1D Linear Regime(≈ 32 K to 52.7 K)

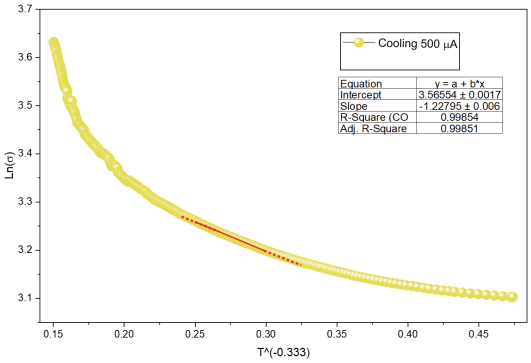

(c) 2D VRH

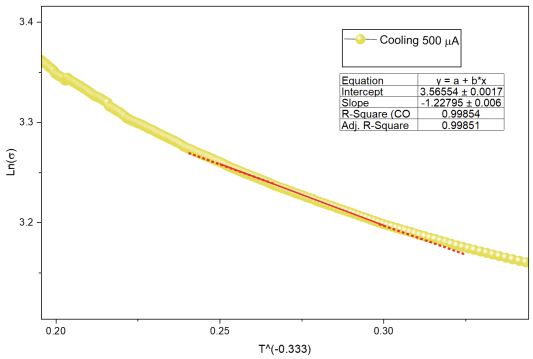

(d) 2D Linear Regime(≈ 37 K to 64 K)

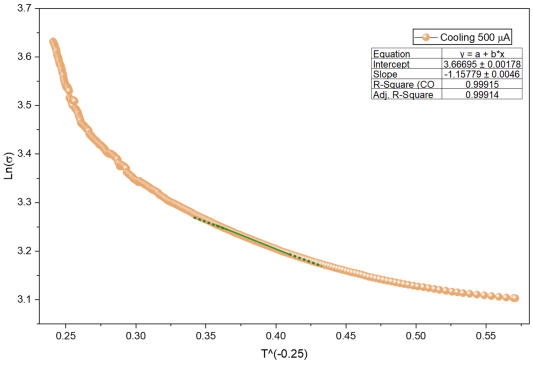

(e) 3D VRH

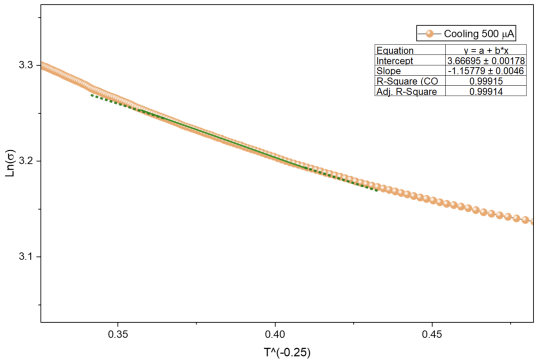

(f) 3D Linear Regime(≈ 35.1 K to 61.3 K)

Figure 5.5: Dimensionality assessment of the 500μA cooling cycle using 1D, 2D, and 3D Variable Range Hopping (VRH) models.

The cooling cycle showed better linearity between temperature 35 K and 61 K for $\alpha = 1/4$ corresponding to the 3D VRH.

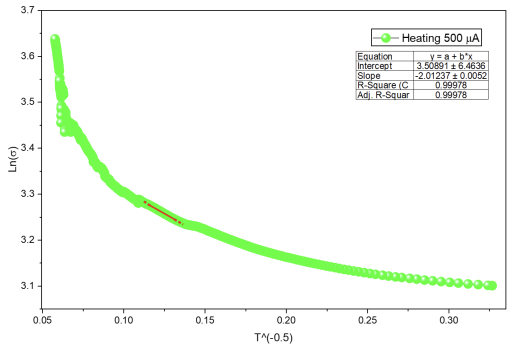

(a) 1D VRH Plot

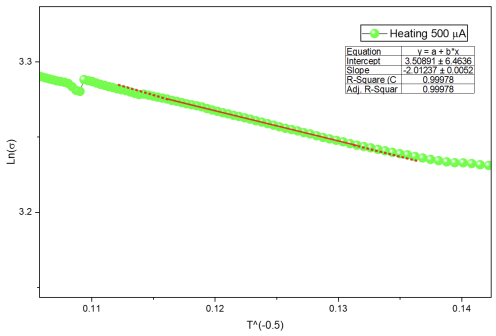

(b) 1D Linear Regime($\approx$ 57.9 K to 74.2 K)

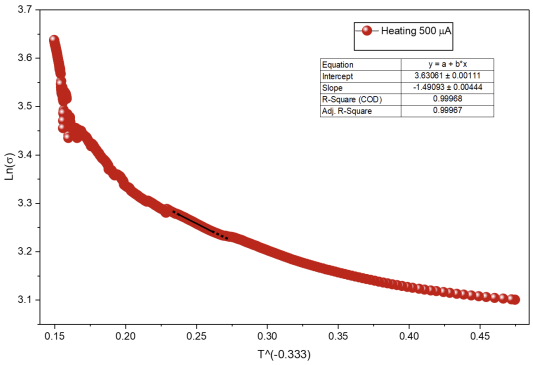

(c) 2D VRH Plot

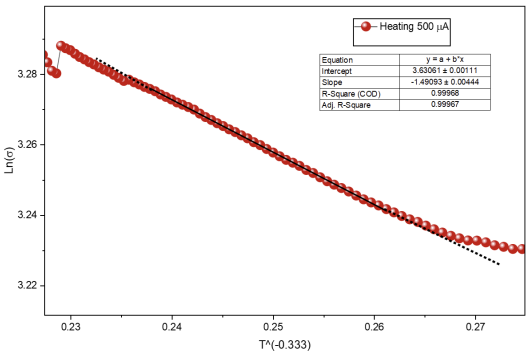

(d) 2D Linear Regime($\approx$ 56.2 K to 74.6 K)

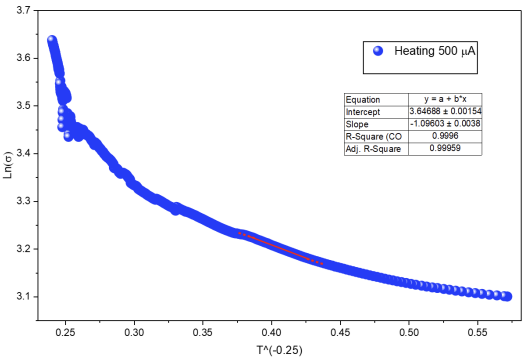

(e) 3D VRH Plot

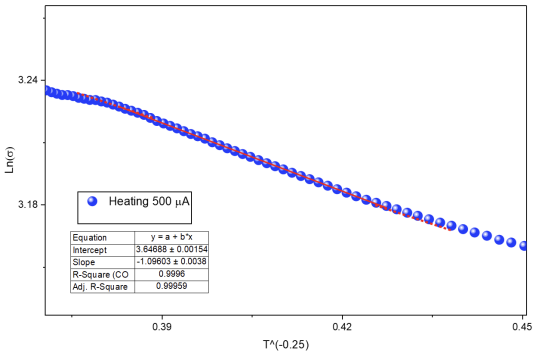

(f) 3D Linear Regime($\approx$ 19.5 K to 46.7 K)

Figure 5.6: Dimensionality assessment of the 500μA heating cycle using 1D, 2D, and 3D Variable Range Hopping (VRH) models.

The heating cycle showed better linearity results between 58 K and 74 K for the $\alpha = 1/2$ case which typically shows 1D VRH behavior. The conduction paths show a tendency toward more confined or restricted paths because thermal expansion and interfacial strain and partial disruption of conductive CNT networks occur during heating.

The linear fits demonstrate their validity only within specific temperature ranges, which do not extend to the entire dataset. The observed differences between heating and cooling cycles demonstrate that thermal history and microstructural changes in the composite material alter its transport behavior. The results demonstrate hopping-based

transport in specific conditions but do not provide enough evidence to identify a single dominant transport mechanism or establish the exact point of dimensionality crossover. The study needs additional methods to achieve its research goals.

The Fe_2O_3@CNT composite material conducts electricity through mechanisms that extend beyond standard semiconducting pathways. The SEM micrographs (Fig. 3.3) reveal a heterogeneous, multi-scale structure that includes conductive pathways created by partially aligned CNT networks together with Fe_2O_3 particles which exist within the nanotubes and additional oxide particles that are located outside the CNT framework. The complex morphology of the material creates multiple pathways for transport, which include conduction through CNT bundles, inter-tube junction hopping, and carrier movement through disordered oxide regions.

The system exists in a non-uniform structural state, which creates multiple conduction pathways that compete with each other instead of producing a single conduction pathway. The interpretation is supported by two findings, which show limited Arrhenius fitting capability and indicate that VRH-like linearity exists only within specific temperature ranges.

Chapter 6

Future Scope

The present study highlights the complex transport behavior of the Fe_2O_3@CNT composite; however, a more comprehensive understanding requires additional experimental and analytical approaches. Future investigations involving temperature-dependent magnetoresistance measurements will help better understand how magnetic ordering functions throughout the Morin transition and affects charge transport.

Temperature-resolved X-ray diffraction (XRD) studies enable us to examine structural changes and lattice distortions that occur with increasing temperature, which will help to identify the relationship between structural changes and transport anomalies. The measurements enable understanding of how Fe_2O_3 encapsulation inside the CNT framework creates strain effects that is observed in the electrical transport data.

From a modeling perspective, we can say that while overall behaviour is semiconducting-like, the exact mechanism of conduction is such hybrids is not clear. Present data rules out a few known conductivity models and brings forward the need of more experimental data as well as theoretical inputs for such novel CNT/Oxide hybrids.

Bibliography

[1] R. H. Baughman, A. A. Zakhidov, and W. A. de Heer, *Science* **297**, 787 (2002).

[2] M. J. Kelly, *Low-Dimensional Semiconductors*, Oxford University Press, New York (1995).

[3] R. Saito, G. Dresselhaus, and M. S. Dresselhaus, *Physical Properties of Carbon Nanotubes*, Imperial College Press, 1998.

[4] H. Dai, "Nanotube Growth and Characterization," in *Topics in Applied Physics*, Vol. 80, p. 29, Springer-Verlag, Berlin (2001).

[5] K. B. K. Teo, C. Singh, M. Chhowalla, and W. I. Milne, in *Encyclopedia of Nanoscience and Nanotechnology*, H. S. Nalwa, Ed., American Scientific Publishers (2004).

[6] R. Saito, M. Fujita, G. Dresselhaus, and M. S. Dresselhaus, *Appl. Phys. Lett.* **60**, 2204 (1992).

[7] C. Kittel, *Introduction to Solid State Physics*, 7th ed., John Wiley, New York (1995).

[8] J. W. Mintmire, B. I. Dunlap, and C. T. White, *Phys. Rev. Lett.* **68**, 631 (1992).

[9] N. Hamada, S. Sawada, and A. Oshiyama, *Phys. Rev. Lett.* **68**, 1579 (1992).

[10] R. Egger and A. O. Gogolin, *Phys. Rev. Lett.* **79**, 5082 (1997).

[11] S. Datta, *Electronic Transport in Mesoscopic Systems*, Cambridge University Press, New York (1995).

[12] L. Forro and C. Schonenberger, in *Carbon Nanotubes: Topics in Applied Physics*, M. S. Dresselhaus, G. Dresselhaus, and P. Avouris, Eds., Springer-Verlag, Heidelberg (2001).

[13] A. Bachtold, C. Strunk, J.-P. Salvetat, J.-M. Bonard, L. Forro, T. Nussbaumer, and C. Schonenberger, *Nature* **397**, 673 (1999).

[14] S. Frank, P. Poncharal, Z. L. Wang, and W. A. de Heer, *Science* **280**, 1744 (1998).

[15] C. Schonenberger, A. Bachtold, C. Strunk, J.-P. Salvetat, and L. Forro, *Appl. Phys. A* **69**, 283 (1999).

[16] P. A. Lee, A. D. Stone, and H. Fukuyama, *Phys. Rev. B* **35**, 1039 (1987).

[17] P. R. Bandaru, *Journal of Nanoscience and Nanotechnology* **7**, 1-29 (2007).

[18] C. Chen, *Magnetism and Metallurgy of Soft Magnetic Materials*, Dover Publications, New York (1986).

[19] M. F. Al-Hakkani, G. A. Gouda, and S. H. A. Hassan, *Heliyon* **7**, e05806 (2021).

[20] S. Kumar, M. Kumar, and A. Singh, "Synthesis and characterization of iron oxide nanoparticles (Fe_2O_3, Fe_3O_4): a brief review" (2021).

[21] B. D. Cullity and C. D. Graham, *Introduction to Magnetic Materials*, 2nd ed. (2009).

[22] D. Givord, "Magnetic properties and magnetic order," in *Encyclopedia of Condensed Matter Physics* (2005).

[23] S. Blundell, *American Journal of Physics* **71**, 94-95 (2003).

[24] M. L. Néel, *Ann. Phys.* **12**, 137-198 (1948).

[25] E. Dzyaloshinskii, *Journal of Experimental and Theoretical Physics* **32**, 1259 (1957).

[26] T. Moriya, *Physical Review* **120**, 91 (1960).

[27] G. Rollmann, A. Rohrbach, P. Entel, and J. Hafner, *Physical Review B* **69**, 165107 (2004).

[28] G. T. Rado and H. Suhl, *Magnetic Ions in Insulators: Their Interactions, Resonances and Optical Properties*, Academic Press, London (1963).

[29] J. Sandon As, J. Baruchel, B. Tanner, G. Fillion, V. Kvardakov, and K. Podurets, *Journal of Magnetism and Magnetic Materials* **104-107**, 350-352 (1992).

[30] A. B. Romanov, *Soviet Physics JETP* **11**, 786 (1960).

[31] M. Keppeler, N. Shen, S. Nageswaran, et al., *J. Mater. Chem. A* **4**, 18223-18239 (2016).

[32] Z. Jian et al., "The magnetic and Color Reflectance Properties of Hematite: From Earth to Mars," *Reviews of Geophysics*, vol. 60, no. 1, 2022.

[33] W. Wu, Z. Wu, T. Yu, et al., *Sci. Technol. Adv. Mater.* **16** (2015).

[34] A. Ali, H. Zafar, M. Zia, et al., *Nanotechnol. Sci. Appl.* **9**, 49-67 (2016).

[35] P. Sharma, S. Dhiman, S. Kumari, et al., *Mater. Res. Express* **6** (2019).

[36] Y. El Mendili, J. F. Bardeau, N. Randrianantoandro, et al., *J. Phys. Chem. C* **116**, 23785-23792 (2012).

[37] B. D. Cullity and S. R. Stock, *Elements of X-Ray Diffraction*, 3rd ed., 2014.

[38] A. Bijelic et al., *ChemTexts*, 2018.

[39] R. Senthil Prabhu et al., "FESEM in pharmaceutical research," *Int. J. Pharm. Biol. Sci.*, 2021.

[40] C. W. Oatley, W. C. Nixon, and R. F. W. Pease, "Scanning electron microscopy," in *Advances in Electronics and Electronic Physics*, vol. 21, p. 181, 1966.

[41] Advanced Research Systems, "Cryocooler Principles of Operation," available at: https://www.arscryo.com/cryocooler-principles-of-operation

[42] Lake Shore Cryotronics, *Model 336 Temperature Controller User's Manual*, Westerville, OH, USA, 2015. Available at: https://www.lakeshore.com/

[43] M. J. Baker, C. S. Hughes, and K. A. Hollywood, "Raman spectroscopy," in *Biophotonics: Vibrational Spectroscopic Diagnostics*, IOP Concise Physics, IOP Publishing, ch. 3, 2014.

[44] A. Cantarero, "Raman Scattering Applied to Materials Science," *Procedia Materials Science*, vol. 9, Dec. 2015. doi: 10.1016/j.mspro.2015.04.014

[45] K. B. Tom, *Graphite oxide template based synthesis and characterization of metal oxide nanosheets*, Doctoral dissertation, University of California, Berkeley, 2015.

[46] A. Kapoor, A. B. Dey, C. Garg, and A. Bajpai, "Enhanced magnetism and time-stable remanence at the interface of hematite and carbon nanotubes," *Nanotechnology*, vol. 30, p. 385706, 2019.

[47] A. Maiti, "Multiscale modeling with carbon nanotubes," *Microelectronics Journal*, 2006. UCRL-JRNL-219435.

[48] A. Ross, R. Lebrun, M. Evers, A. Deák, L. Szunyogh, U. Nowak, and M. Kläui, "Exceptional sign changes of the nonlocal spin Seebeck effect in antiferromagnetic hematite," *Physical Review B*, vol. 103, p. 224433, 2021.

[49] V. P. Prasadam, *Functional coatings based on MWCNT-metal oxide nanocomposite for solar energy harvester application*, Ph.D. dissertation, University of Luxembourg, Esch-sur-Alzette, Luxembourg, 2021.

[50] A. B. Kaiser et al., "Variable range hopping and/or phonon-assisted tunneling mechanism of electronic transport in polymers and carbon nanotubes," *Cent. Eur. J. Phys.*, 2012.

[51] K. G. Lisunov, E. Arushanov, H. Vinzelberg, G. Behr, and J. Schumann, *J. Appl. Phys.*, vol. 97, p. 093706, 2005.

[52] M. Ghosh, A. K. Meikap, S. K. Chattopadhyay, and S. Chatterjee, *J. Phys. Chem. Solids*, vol. 62, p. 475, 2001.

[53] Y. Long et al., *Phys. Rev. B*, vol. 71, p. 165412, 2005.

[54] A. C. Ferrari and D. M. Basko, "Raman spectroscopy as a versatile tool for studying the properties of graphene," *Nature Nanotechnology*, vol. 8, p. 235, 2018.

[55] M. S. Dresselhaus, A. Jorio, and R. Saito, "Characterizing graphene, graphite, and carbon nanotubes by Raman spectroscopy," *Annual Review of Condensed Matter Physics*, vol. 1, p. 89, 2010.

[56] A. A. Ismail, A. M. Ali, F. A. Harraz, M. Faisal, H. Shoukry, and A. E. Al-Salami, "A facile synthesis of α-Fe_2O_3/carbon nanotubes and their photocatalytic and electrochemical sensing performances," *International Journal of Electrochemical Science*, vol. 13, 2018.

[57] V. Modafferi, M. Fiore, E. Fazio, S. Patanè, C. Triolo, S. Santangelo, R. Ruffo, F. Neri, and M. G. Musolino, "Synthesis and characterization of Fe_2O_3/reduced graphene oxide nanocomposite as a high-performance anode material for sodium-ion batteries," *Journal of Power Sources*, 2022.

[58] N. Yan, X. Zhou, Y. Li, F. Wang, and H. Zhong, "Fe_2O_3 Nanoparticles Wrapped in Multi-walled Carbon Nanotubes With Enhanced Lithium Storage Capability," *Scientific Reports*, vol. 3, p. 3392, 2013.

[59] Royal Society of Chemistry, "Electronic Supplementary Material (ESI) for RSC Advances," 2023. This journal is © The Royal Society of Chemistry 2023.

[60] I. G. Austin and N. F. Mott, "Polarons in crystalline and non-crystalline materials," *Advances in Physics*, vol. 18, no. 71, pp. 41–102, 1969.

[61] M. Jeníková, K. Zakuťanská, J. Kováča, V. Girman, P. Kopčanský, and N. Tomašovičová, "Characterization of Carbon Nanotubes," in *Proceedings of the 16th Czech and Slovak Conference on Magnetism*, Košice, Slovakia, June 13–17, 2016.

[62] A. N. Mohan, B. Manoj, and A. V. Ramya, "Probing the nature of defects of graphene like nano-carbon from amorphous materials by Raman spectroscopy," *Asian Journal of Chemistry*, vol. 28, no. 7, pp. 1501–1504, 2016.